

1 20170727: DARK MATTER SEARCH AND ELECTRON BACKGROUND
2 EVALUATION
3 TESTING OF TPC GRID DESIGNING

4 A DISSERTATION
5 SUBMITTED TO THE DEPARTMENT OF PHYSICS
6 AND THE COMMITTEE ON GRADUATE STUDIES
7 OF STANFORD UNIVERSITY
8 IN PARTIAL FULFILLMENT OF THE REQUIREMENTS
9 FOR THE DEGREE OF
10 DOCTOR OF PHILOSOPHY

11 Wei Ji
12 July 2018

¹³

© Copyright by Wei Ji 2018
All Rights Reserved

¹⁴

I certify that I have read this dissertation and that, in my opinion, it is fully adequate in scope and quality as a dissertation for the degree of Doctor of Philosophy.

15

(Tom Shutt) Principal Adviser

I certify that I have read this dissertation and that, in my opinion, it is fully adequate in scope and quality as a dissertation for the degree of Doctor of Philosophy.

16

(Dan Akerib)

I certify that I have read this dissertation and that, in my opinion, it is fully adequate in scope and quality as a dissertation for the degree of Doctor of Philosophy.

17

(Peter Graham)

I certify that I have read this dissertation and that, in my opinion, it is fully adequate in scope and quality as a dissertation for the degree of Doctor of Philosophy.

18

(Giorgio Gratta)

I certify that I have read this dissertation and that, in my opinion, it is fully adequate in scope and quality as a dissertation for the degree of Doctor of Philosophy.

19

()

Approved for the Stanford University Committee on Graduate Studies

20

²¹ Preface

²² This thesis is discussing about the design and validation of liquid xenon LZ Dark Matter experiment
²³ and results from LUX Dark Matter experiment.

²⁴ **Acknowledgments**

²⁵ I would like to thank you Dan, for everything.

²⁶ Contents

²⁷ Preface	iv
²⁸ Acknowledgments	v
²⁹ List of Tables	vii
³⁰ List of Figures	viii
³¹ 1 Gas Test descriptions	1
³² 1.1 The gaseous detector	2
³³ 1.2 Data Acquisition	5
³⁴ 1.3 Operation	11
³⁵ 1.4 Data processing	14
³⁶ 1.5 PMT Calibration	16
³⁷ 1.6 Light Collection	19
³⁸ 1.7 Light production	26
³⁹ 1.8 Events	30
⁴⁰ 1.9 Cuts	32
⁴¹ 1.9.1 Coincidence found	33
⁴² 1.9.2 Uncorrelated from preceding pulses	34
⁴³ 1.9.3 Pulse shape	36
⁴⁴ 1.10 Evaluation	39
⁴⁵ 1.10.1 Simulations	39
⁴⁶ 1.10.2 Summary	39
⁴⁷ A Gas Test RQ documentation	44
⁴⁸ B Abbreviations	51
⁴⁹ Bibliography	53

⁵⁰ List of Tables

⁵¹ 1.1	Spectral response of PMTs tested by Hamamatsu Photonics	5
⁵² 1.2	Data Acquisition system parameters.	8
⁵³ 1.3	PMT dead time duration	11
⁵⁴ 1.4	PMT calibration.	19
⁵⁵ 1.5	Light collection simulation geometry parameters.	22
⁵⁶ 1.6	Light collection simulation material parameters.	23
⁵⁷ A.1	<i>Gas Test</i> RQ documentation	50

⁵⁸ **List of Figures**

⁵⁹ 1.1	<i>Gas Test</i> electroluminescence detector.	4
⁶⁰ 1.2	<i>Gas Test</i> apparatus physical layout.	6
⁶¹ 1.3	<i>Gas Test</i> data acquisition system physical layout.	7
⁶² 1.4	Distribution of PMT time intervals between consequential pulses.	10
⁶³ 1.5	<i>Gas Test</i> good and bad voltage configurations.	13
⁶⁴ 1.6	PMT pulse amplitude distribution.	18
⁶⁵ 1.7	PMT SPHE pulse amplitude vs pulse area distribution.	20
⁶⁶ 1.8	Light collection efficiency of rz cross section in the ELD.	24
⁶⁷ 1.9	Light collection efficiency in the EL region with different configurations.	25
⁶⁸ 1.10	Light collection efficiency in the EL region with different PTFE reflectivity/	25
⁶⁹ 1.11	The reduced first Townsend ionization coefficient $\eta \equiv \alpha/E$ for neon, argon, krypton, and xenon.	29
⁷¹ 1.12	<i>Gas Test</i> electron emission event from grid wires	31
⁷² 1.13	<i>Gas Test</i> anode cone event	41
⁷³ 1.14	<i>Gas Test</i> extremely narrow event	42
⁷⁴ 1.15	<i>Gas Test</i> extremely narrow event: coincidence pulse duration vs coincidence pulse area	43

⁷⁵ **Chapter 1**

⁷⁶ ***Gas Test descriptions***

⁷⁷ In LZ, metallic wire grids under high voltage are used to form electric fields. We apply one field
⁷⁸ in the liquid volume to drift ionization electrons upwards and another in the gas volume to extract
⁷⁹ these electrons from the liquid in order to produce proportional scintillation light (S2). Achieving
⁸⁰ high voltages on such grids is necessary for the operation of the LZ TPC. However, such high voltages
⁸¹ also increase the rate of electron emission which is one of the potential sources of background in
⁸² LZ. Therefore, reduction of the field induced electron emission rate should greatly benefit physics
⁸³ studies in the LZ detector.

⁸⁴ Electric field induced electron emission from metallic surfaces is a well known phenomenon. The
⁸⁵ electric field lowers the potential energy outside the metallic surface allowing electrons to come out
⁸⁶ from the metallic surface. The rate of electric field induced electron emission increases with the
⁸⁷ electric field on the metallic surface.

⁸⁸ The electric field induced electron emission events are potential problems in LZ for three reasons.
⁸⁹ First, these events look like low energy events in the LZ detector. Thus, reduction of electron
⁹⁰ emission background rate from the grid wires improves our sensitivity to low energy events. This in
⁹¹ return improves our ability to study low mass WIMPs. Second, the electron emission events may
⁹² accidentally coincide with wanted WIMP signals in the LZ detector. Reduction of electron emission
⁹³ rate helps to keep the data recording environment in LZ cleaner. This reduces the systematic errors
⁹⁴ for S1 and S2 and improves their quality. From that, we improve our events classification and energy
⁹⁵ reconstruction. This in turn improves all physics studies from the LZ detector. Finally, the electron
⁹⁶ emission events consume data recording ability in LZ. This may prevent or interrupt recordings of
⁹⁷ wanted data. Thus, reduction of electron emission rate helps to keep the data recording environment
⁹⁸ in LZ quieter to allow longer detector live times for wanted events. In summary, reduction of the
⁹⁹ electron emission event rates benefits LZ in detector sensitivity, data quality and data acquisition
¹⁰⁰ live time.

¹⁰¹ To achieve these quality, we are developing a two-stage study on reduction of the electric field

102 induced electron emission rate using two small detectors, *Gas Test* and *LZ System Test: Phase I*.
103 These two detectors are capable of testing a pair of grids which have surface areas $\sim 1\%$ the area of
104 grids that will be used in LZ. With these small detectors, we can study the effect of rate reduction
105 in a shorter time than if we were to use full-size grids. Thus, we use these detectors to quickly study
106 parameters that may affect the emission rate.

107 In the first stage, a gaseous detector, “*Gas Test*”, is built to study different methods for reducing
108 the electron emission rate. This detector measures electron emission rates with different electric
109 fields before and after various physical and chemical treatments. Once we discover an effect on
110 reduction of the electric field induced electron emission rate from these treatments, a second stage
111 of study with a liquid xenon detector, *LZ System Test: Phase I*, is done to confirm that reduction
112 persists in a liquid xenon environment, like that of LZ.

113 After confirmation that a treatment produces a rate reduction, this treatment is used to produce
114 full-size LZ grids. A similar two-stage study method is used to test the full-size LZ grids in a gaseous
115 detector, *LZ System Test: Phase II* (details are described in Ref. ??), and the liquid xenon detector
116 LZ. These two detectors measure the performance and assure the quality of LZ grids.

117 This chapter focuses on descriptions of the *Gas Test* detector. I will first introduce the design
118 concepts for each individual component in *Gas Test*. Then I will discuss data acquisition and the
119 data processing framework. **Last, I will discuss the analysis framework which includes event selec-**
120 **tions , simulations and validations, as well as characteristic pulse shape and rate of the background**
121 **events.** Results from measurements for different grids in *Gas Test* will be discussed in Chapter.??.

122 1.1 The gaseous detector

123 The gaseous detector, *Gas Test*, is designed for studying grid behavior under high voltage for LZ. It
124 measures scintillation and electroluminescence (EL) light signals from events in the detector. Pairs
125 of grids are made with the same waving technique, material, wire pitch, and wire diameter as the
126 grids that will be used for LZ. The differences between these grids and grids in LZ are the diameters
127 of the grid planes. The same pair of grids can also be tested in *LZ System Test: Phase I* for studying
128 their performance in liquid xenon. Since these grid are physically similar to LZ except for the overall
129 surface area, the results from studying these grids are an useful guidance for LZ grid design.

130 A study is done on understanding the maximum operation voltage and the optimal operation
131 voltage by grid sparking tests. Grid sparking tests are performed with both gaseous xenon and argon
132 in various pressures. It is to look for discharging in the detector with biasing the grids. It provides
133 the detector operation informations for grid emission tests.

134 Electron emissions from the grid wires are studied by grid electron emission tests. Grid electron
135 emission tests are usually performed with gaseous xenon at 0.137 mol L^{-1} ($\sim 3.3 \text{ bara}$ at temperature
136 295 K). Grid electron emission tests look for electron emission pulse from grids with PMTs.

137 **Detector** The detector operates with xenon gas, argon gas, and vacuum. Operation pressure for
138 this detector is in range 10^{-5} bara to 3.5 bara.

139 A cylinder vessel of 10 inch diameter and 24 inch height is used to host electroluminescence
140 detector. Pressure and temperature of the detector are monitored by sensors mounted above the
141 vessel. A gas circulation system is used to add, remove and purify gas for the detector. Fig. 1.2a and
142 Fig. 1.2b show the physical layout of the vessel setup and the electroluminescence detector inside.

143 The electroluminescence detector (ELD) is the major location of active measurable events. Its
144 conceptual drawing is illustrated in Fig. 1.1. A pair of grids for measurement are mounted in the
145 center of the vessel. They are separated apart by 13 mm by 12 PEEK spacers. These two grids are
146 biased to different voltages during the measurement. This creates an operation voltage difference
147 between the two grids. It enables electrons between these two grids to produce EL photons which
148 can be measured by the PMTs. The region between these two grids is called EL region.

149 These grids are named after their physical location in the detector as top grid and bottom grid.
150 The grid plane diameters are 140.9 mm for the top grid and 137.4 mm for the bottom grid. Voltages
151 of the two grids are noted as V_T for the top grid and V_B for the bottom grid. The voltage difference
152 between the top and bottom grid is noted as operation voltage $dV \equiv V_T - V_B$. They also have
153 another name by their bias voltage. The more anodic grid is called anodic grid. The more cathodic
154 grid is called cathodic grid. Their voltage are also sometimes noted as V_A for the anodic grid and
155 V_C for the cathodic grid. Normally, the top grid is anodic and the bottom grid is cathodic to study
156 electron emission from the bottom grid. This is normal polarity operation. Occasionally, the top
157 grid is cathodic and bottom grid is anodic to study electron emission from the top grid. This is
158 reverse polarity operation.

159 Two PTFE reflector cones are used to improve light collection efficiency for the primary scin-
160 tillation and EL photons. These reflector cones are mounted on the top and bottom of the EL
161 region. The surface of PTFE cones overhang 0.1 mm above the grid. The diameters of the opening
162 of the PTFE cone to the grids are 130 mm. Light collection will have the most sensitivity for grid
163 electron emission pulse in this region. This defines the overall grid surface area of studying. Two
164 PMTs mounted on the PTFE reflector cones are used to measure the primary scintillation and EL
165 photons. Distances between the PMTs to the closest grids are 110 mm.

166 A CAEN R1470ETD high voltage power supply is used to bias the two grids and the two PMTs.
167 Two custom ceramic feed throughs are used to deliver high voltage into the detector vessel to
168 the two grids. Each feed through has a low-pass filter box attached for noise removal. Custom
169 designed cables and cable terminations are used to transfer power between the feed throughs and
170 the grids. The cable terminations had limited us biasing grids to high voltage. Improvements of
171 designs are established to solve this problem. Details of iterations of these designs will be discussed
172 in Chapter. ??.

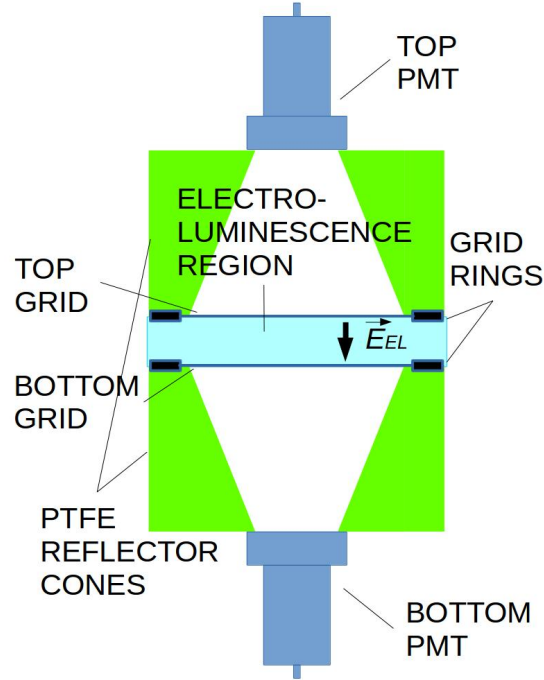


Figure 1.1: Conceptual drawing of *Gas Test* electroluminescence detector (ELD)

173 **Gas circulation system** A gas circulation system is used for adding, removing, purifying xenon
 174 gas in the detector. The circulation system also is used to maintain gas purity condition. It removes
 175 impurity atoms such as oxygen, water, and hydrocarbons. The purity of xenon gas makes sure
 176 that electrons that is created in ELD do not combine with impurity atoms, thus been prevented to
 177 produce EL light. The purity of xenon also has an notable effect on electron drift velocity in xenon
 178 gas. Impure xenon gas tend to have a slower drift velocity. The deviation of drift velocity between
 179 different impurity level can reach 20 % at certain reduced electric field (ratio of electric field to gas
 180 density), as described in Ref. ??.

181 Xenon purification is done through circulating xenon gas through a getter purifier. A gas cir-
 182 culation panel is used to control the flow of xenon gas. A SAES PS3-MT3-R-1 rare gas purifier
 183 getter mounted on the circulation panel is used to purify the gas. The getter element has a sub-
 184 ppb efficiency of removing water, nitrogen, oxygen, carbon oxide, carbon dioxide, hydrogen, and
 185 hydrocarbons, as described in Ref. [1]. A custom pump manufactured by KNF Neuberger, Inc. is
 186 used to drive the gas circulation in the system. This pump is a type PM26101-0150.1.2.12 double
 187 diaphragm pump, which has company specified 1.5 bar operation pressure, as described in Ref. [2].
 188 During the actual operation, the pump is working at pressure up to 3.7 bar. The diaphragm pump

	Top(top) PMT	Bottom(bot) PMT
Serial Number	KB1163	KB1170
Cathode Luminous Sens. [$\mu\text{A lm}^{-1}$]	149.0	148.0
Anode Luminous Sens. [A lm^{-1}]	657.0	1010.0
Anode Dark Current [nA]	1.00	4.60
Cathode Blue Sens. Index	12.60	12.30
Q.E. [%]		
165 nm	22.1	21.2
170 nm	33.3	32.6
175 nm	36.3	36.0
182 nm	37.1	37.0
188 nm	36.1	36.2
194 nm	33.9	34.1
200 nm	32.6	32.9

Table 1.1: Spectral response of PMTs tested by Hamamatsu Photonics.

189 shows a leak rate less than 10^{-7} bar L s $^{-1}$. The circulation flow rate is controlled by a Alicat MC-
 190 5SLPM-D-485 mass flow controller on the gas circulation panel. It allows a maximum flow rate at
 191 5 slpm, as described in Ref. [3]. Fig. 1.2c shows the gas circulation panel.

192 Two 4 L bottles are used for the storage of xenon gas used in the tests. These bottles are can
 193 be inserted to two dewars. The dewars are filled with liquid nitrogen during removing xenon gas
 194 process. Reducing the temperature of the bottle by liquid nitrogen allows xenon to flow back to and
 195 condense inside the bottles. During adding xenon gas process, the bottles are taken out from the
 196 dewar and warmed up. Fig. 1.2d shows the pump and storage bottles for the detector.

197 **PMT** Two PMTs are used to measure the primary scintillation and EL photons from events
 198 happens in the detector. Both PMTs are model R11410-20 PMTs manufactured by Hamamatsu
 199 Photonics, as described in Ref. [4]. The PMTs are named after their physical location in the detector
 200 as top PMT and bottom(bot) PMT. The spectral response of the PMTs tested in Hamamatsu
 201 company is summarized in Table. 1.1.

202 1.2 Data Acquisition

203 A data acquisition(DAQ) system is used for recording PMT pulses for grid emission tests. The DAQ
 204 system is designed and made in SLAC, previous used and tested in *LZ System Test: Phase I* . The
 205 DAQ system is customized to maximize the probability for capture single photon electron (SPHE)
 206 pulses from the PMTs. This also enables the DAQ system to record electron emission pulses, which
 207 are collections of multiple SPHEpulses. The DAQ system contains three parts: (1) amplification
 208 and digitization, (2) recording, and (3) transfer and storage. The DAQ system works continuously,



Figure 1.2: *Gas Test* apparatus physical layout: (a) the *Gas Test* detector: detector vessel (middle), electronic and gas gauge breakouts (top), Jenny lift for detector assembly and disassembly (left), and vacuum pumping and leak check system (right), (b) ELD inside the detector vessel, (c) gas circulation panel, (d) circulation pump (left), and storage bottles (right).

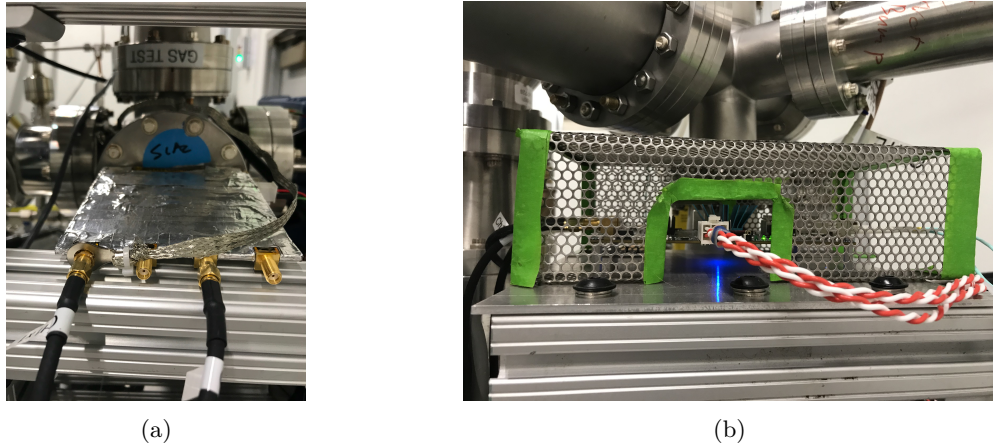


Figure 1.3: *Gas Test* data acquisition system physical layout: (a) amplifier board. (b) digitizer board.

209 except for interrupted by data transfer. This interruption is called dead time of the DAQ system.
 210 The dead time issue in studies of electron emission pulses is addressed by subtraction of live times
 211 after each recorded pulses. Aspects of the DAQ system is described below.

212 **Amplification and digitization** The amplification and digitization system amplifies and digitizes
 213 PMT pulse signals. The amplification and digitization of the PMT signals are done by two separate
 214 custom made boards. The amplification board amplifies signals so that it improved signal to noise
 215 ratio. There are two amplifier gain settings implemented: low gain ($\times 12$), and high gain ($\times 100$).
 216 For electron emission tests, the low gain setting is used to get enough signal to noise ratio. The low
 217 gain setting allows 40 to 60 SPHEs to be recorded simultaneously without distortion, as described
 218 later in Section 1.5. The high gain setting is not used because its without distortion SPHE recording
 219 range is 5 to 7 SPHEs, which is too small for the counts of simultaneous SPHEs in electron emission
 220 pulses. An optical fiber connecting these two boards transfers the amplified PMT signals to the
 221 digitizer board. The digitizer board is capable of doing a 16 bit digitization in a dynamic range
 222 of 2.5 V. The actual range of digitizing voltage is ~ -1.26 V to 1.24 V. The digitizer reverses
 223 the polarity of signals, which changes SPHE pulses from negative spikes to positive spikes. The
 224 digitizing sampling frequency is every 4 ns. Digitized data are written to a buffer memory in the
 225 digitizer board. The amplification and digitization system sets the precision of SPHE measurement
 226 and signal to noise ratio, and digitizes PMT pulse signals to be handled numerically later.

227 **Recording** The recording system for DAQ makes decisions for data recording. The decision
 228 making algorithm is controlled by customized DAQ XML parameters in an XML file. The pulse
 229 recording is done in a pending mode without a conventional trigger, which is explained below. First,
 230 the continuous digitized pulse amplitude data are compared to a pre threshold voltage (trigger

name	XML parameter name	value	explanation
post delay	'PostDelay'	500 sample	counts of samples to keep after crossing post trigger threshold ('PostThreshold').
pre delay	'PreDelay'	30 sample	counts of samples to keep before crossing pre trigger threshold ('PreThreshold').
post threshold	'PostThreshold'	0x7D80 or as needed	crossing this threshold value determines the stop time of pulse recording.
pre threshold	'PreThreshold'	0x7D61 or as needed	crossing this threshold value determines the start time of pulse recording.

Table 1.2: DAQ system parameters. (1 sample is 4 ns.)

voltage), which is called pre threshold value, until finding a threshold crossing. The time of this threshold crossing is the pulse recording reference time. Pulse recording also includes a preceding segment of samples, which is called pre delay. The earliest time of pre delay period is the pulse recording start time. Next, digitized data are compared to a post threshold voltage, which is called post threshold value, until finding a threshold crossing. Then, pulse recording continues for a succeeding segment of samples, which is called post delay. During the post delay period, the digitized data are compared to the pre threshold again. If no pre threshold crossing is found, pulse recording ends when the post delay period ends. Otherwise, the DAQ system keeps recording until after a post threshold crossing, no other pre threshold crossing can be found in the next post delay period. The latest time of the last post delay period is the pulse recording stop time. The pre threshold values are chosen so that the SPHE recording efficiencies, also called trigger efficiencies, of both PMTs are larger than 95 %. The trigger efficiencies are estimated by fitting SPHE amplitude distributions to Gaussian distributions. Results of these evaluations show that at normal PMT operation voltage (-1.5 kV) the top PMT and the bottom PMT have good trigger efficiencies of 99.6 % and >99.9 %. The recorded pulses are called pulses of digitization (PODs), which are one of the fundamental elements for the next step coincidence event building.

The default settings for the DAQ XML parameters are summarized in Table 1.2.

Transfer and storage The transfer and storage system transfers data from the digitizer board and stores data in binary format in a main computer. The buffer memory data pass the selection of trigger algorithm are transferred through an optical fiber and written to the main computer. Data transfer speed is 250 MB s^{-1} . For an average pulse duration of $2\mu\text{s}$ (500 sample), the DAQ allows approximate 30 thousand pulses to be recorded per second. The continuously recorded data are separately saved to series of files with maximum size of 1.1 GB. Data transfer interrupts buffer

254 memory writing of the succeeding digitized data, which raises the dead time issue.

255 **Dead time** The dead time of DAQ is the segment of time that the DAQ system stops working
 256 after the end of each recording. The reason for the dead time is because buffer writing and data
 257 transfer in the DAQ system cannot happen at the same time. Dead time issue brings challenges on
 258 measuring electron emission rates. Duration of dead time shows a dependence on the preceding pulse
 259 duration and pulse size. However, the quantitative relationship between duration of dead time and
 260 the two is unclear. We address this issue by subtracting a segment of time preceding each recorded
 261 pulse from the live time of study.

262 We studied the dead time issue with two methods. The first method is finding potential dead time
 263 problematic pulses that have no recording in one PMT when there are large quantities of photons
 264 recorded by the other PMT at the same time. Since the two PMTs are geometrically looking at the
 265 same region in the ELD, we expect to see similar magnitude of photons in both PMTs. The most
 266 likely reason for the no recording in one PMT is this PMT is suffering from the dead time issue.
 267 The other causes of these problematic pulses, such as misbehavior of one PMT, are less dominant.
 268 The time difference between the large quantities of photons recording time in the other PMT and
 269 the first preceding pulse in the dead time problematic PMT is the potential duration of dead time.
 270 More than 400 dead time problematic pulses are examined. From the examinations, we found for a
 271 pulse with a duration of $2\ \mu\text{s}$, duration of dead time is in range $0.3\ \mu\text{s}$ to $15\ \mu\text{s}$. For longer pulses,
 272 we observe dead time as long $80\ \mu\text{s}$.

273 To estimate the systematic error, we employ a second method based on the idea that the presence
 274 of dead time will shift the distribution of time intervals between pulses in one PMT. In the absence
 275 of dead time, the time distribution should be an exponential characterized by the average rate.
 276 The impact of dead time is to shift time difference probability an exponential curve, which is from
 277 assuming uniform distribution:

$$\text{probability} = \frac{1}{\tau} \exp\left(-\frac{t}{\tau}\right) \quad (1.1)$$

278 where τ is the time constant, which is the inverse of average rate.

279 Results of this shift is shown in Fig. 1.4. The figure includes studies of pulses categorized by
 280 their durations. These studies confirm the previous conclusion on the dead time issue dominant
 281 period, and further show that such period has a dependence on the preceding pulse duration. The
 282 clear low statistics at the small time interval range, e.g. range 0 ns to 10^5 ns for pulse length in range
 283 larger than $30\ \mu\text{s}$, clearly showed the shift from expected exponential curve. The low statistic region
 284 changes with preceding pulse duration, as summarized in Table. 1.3. The difference on the slopes
 285 of these curves is due to PTFE fluorescence subsequent to each pulse, which is more obvious for
 286 larger area (long duration) pulses, and increases the succeeding average rate, as will be discussed in
 287 Section. 1.8.

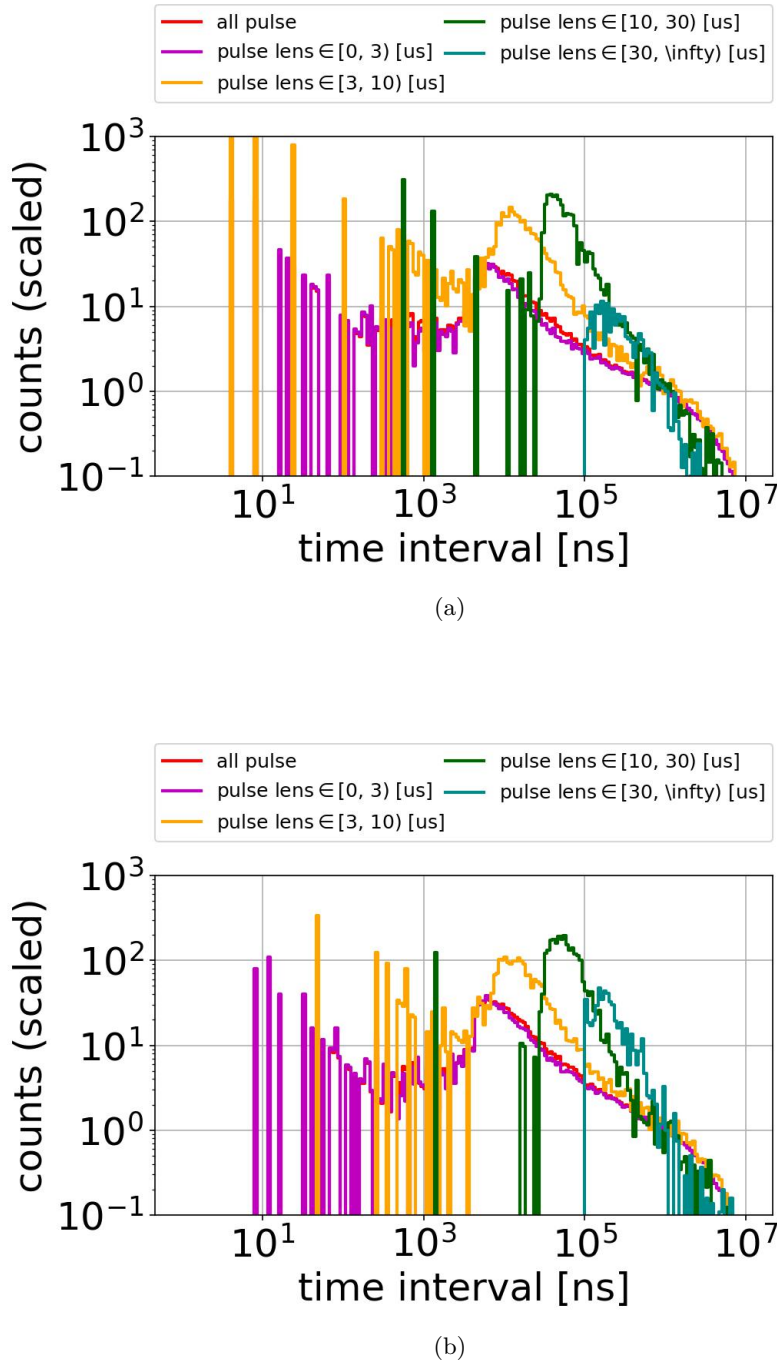


Figure 1.4: Distribution of PMT time intervals between consequential pulses.: (a) top PMT (b) bottom PMT. Data were taken at 2017-12-8 14:02, with operation voltages V_T and V_B at +6 kV and -6 kV, operation detector gas density at 0.137 mol L^{-1} .

pulse length [μs]	dead time duration (low statistics region) [μs]	dead time duration (maximum observed) [μs]
all	7	80
[0, 3)	7	15
[3, 10)	10	15
[10, 30)	50	80
[30, ∞)	100	80

Table 1.3: PMT dead time duration. Data were taken at 2017-12-8 14:02, with operation voltages V_T and V_B at +6 kV and -6 kV, operation detector gas density at 0.137 mol L^{-1} .

288 Thus, to resolve the dead time issue, we subtract a segment of time after each recorded pulse
 289 from the live time of study and eliminate all pulses that is recorded in this time period, as described
 290 in Section 1.9. The remained pulses that have quiet preceding are used to study the absolute rate
 291 of signals of interest, electron emission pulses. The rate of signals of interest is close to such rate
 292 without the dead time issue from the view of DAQ behavior.

293 1.3 Operation

294 think about where to put run selection section. I want to take about , what is sparking test, what
 295 is normal operation before electron emission tests. This is the reason this section is here. however,
 296 put it just in front of cut might also be good.

297 The run selections are to make sure that we have stabilized run conditions to analysis electron
 298 emission process from grids we are studying.

299 **Operation conditions** The normal run of *Gas Test* electron emission test is operated with (1)
 300 the detector filled with xenon gas, (2) two PMTs stably running, and (3) two grids bias to proper
 301 voltages.

302 The typical operation xenon gas density for electron emission tests is 0.137 mol L^{-1} (or equivalent
 303 to the xenon gas density at 177 K on xenon liquid-vapor saturation curve). This choice is made
 304 to have the gas density closest to LZ operation gas density. It also minimizes the probability of
 305 discharges between two grid electrodes. These discharges may cause potential damages to grids, and
 306 also prevent stable run.

307 The gas operation condition at density 0.137 mol L^{-1} allows us having sensitivities measuring
 308 electron emission from operation voltage dV in range 8 kV to 16 kV. For a plain woven grid with
 309 wire pitch 5 mm and wire diameter $75 \mu\text{m}$, this correspond to an average wire surface electric field
 310 in range 65 kV cm^{-1} to 110 kV cm^{-1} . However, since EL yield decreases as the reduced electric
 311 field (ratio of electric field to gas density) in the EL region decreases, the photon yield per electron
 312 emission is smaller for a lower operation voltage dV . This prevents us to have enough sensitivities for

313 electron emission for a lower operation voltage and wire surface electric field . So electron emission
 314 rate for a lower wire surface electric field is measured at a lower gas density to get an increasing
 315 on the reduced electric field and the EL photon yield in gas. The EL yield dependence on reduced
 316 electric field is described in Section. 1.8.

317 Two PMTs normally operate at -1.5 kV . This guarantees both PMTs having enough gain and
 318 signal to noise ratio. Before safely turning on the PMTs to measure the light emission from the grids,
 319 a series of sparking tests are done to figure out the high voltage behavior and high voltage weak
 320 points in the system. Improvements are done to improve the maximum operation voltages V_T and
 321 V_B . These improvements include cleaning the surface of discharging spots, increasing the smoothness
 322 and rounding radius on the corner of metal surfaces, and increasing the discharge distance between
 323 electrodes and the ground. Touching grid wires are avoided during these improvements. The max-
 324 imum operation voltages V_T and V_B that these grids can hold are measured with different gas and
 325 different pressures. Dark current of both PMTs in stable running condition are approximately 500 Hz
 326 to 1000 Hz. Runs with any PMT dark current rate above 2500 Hz are excluded.

327 The high voltage power supply is capable to bias both grids separately in range -8 kV to 8 kV .
 328 The current between the power supply and the grid is monitored to guarantee stable operation of
 329 grid bias voltage. An unstable grid biasing usually shows as a spike in the monitored current, and a
 330 spike on PMT recording rates. Segments of time with this monitored current unstable are excluded.

331 **Operating data taking** The most common operation voltage pairs we choose for electron emission
 332 measurement at xenon gas density 0.137 mol L^{-1} are $V_T = -V_B$ at $\pm 4\text{ kV}$, $\pm 4.5\text{ kV}$, $\pm 5\text{ kV}$, $\pm 5.5\text{ kV}$,
 333 $\pm 6\text{ kV}$, $\pm 6.5\text{ kV}$, $\pm 7\text{ kV}$, $\pm 7.5\text{ kV}$, and $\pm 8\text{ kV}$. This allows us to measure electron emission rate vs
 334 operation voltage dV curves for most grids we study. Measurements in other conditions are also
 335 performed to understand the detector better. However, their results usually are not included for the
 336 electron emission studies.

337 The typical duration of data taking is three minutes. An increasing trend of light production is
 338 seen during the operations when data taking is longer than three minutes. This is probably from
 339 the increasing of EL light production from the more ionized chamber environment and increasing
 340 of fluorescence light emission from PTFE reflector cones in the detector. Usually, after each 3 min
 341 dataset, high voltage power for both grids are set back to 0 kV and rest for at least 30 s before the
 342 next measurement. Data taking at each voltage configuration is handled by using scripts in Ignition
 343 slow control software, as described in Ref. ???. This is to make sure data taking is done in a consistent
 344 reproducible way.

345 Datasets with the lower value of two grid bias voltages higher than -2.5 kV are explicitly excluded
 346 for electron emission measurements. The reason is because this configuration allows electrons created
 347 by external particle in the cone region drifting to the EL region. These electrons will produce EL
 348 light in the EL region. This could introduce a background for electron emission rate study. The
 349 process is illustrated in Fig. 1.5.

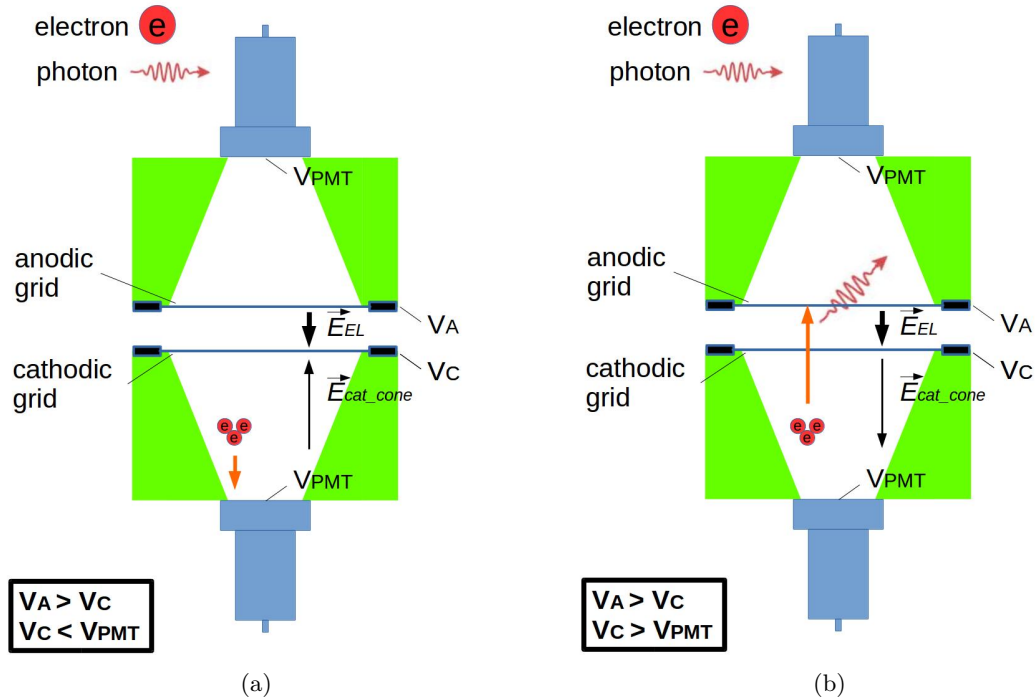


Figure 1.5: (a) good configuration ($V_C < V_{PMT}$) : drift field is pointing from PMT to the grids. Electrons created in the cone region will drift to PMT. This process do not create as many photons as electron emission pulse. (b) bad configuration ($V_C > V_{PMT}$) : drift field are pointing from grids to the PMT. Electrons created in the cone region will drift to EL region. This process create lots of EL photons and could look like an electron emission pulse.

350 1.4 Data processing

351 Data processing is to save the useful informations of data by reducing the amount of extraneous
 352 informations. This reduces size of analysis works. The useful informations of a pulse are characterized
 353 by Reduce Quantities of a pulse (RQs).

354 The data processing framework include three parts: (1) single pulse processing, (2) coincidence
 355 event building and coincidence pulse processing, and (3) random segment sampling of the dataset.

356 This section explains the main part of data processing framework. It does not mean to explain
 357 all the RQs that have been computed. A full documentation of the RQs used in *Gas Test* analysis
 358 is summarized in Appendix. A.

359 **Single pulse processing** A single pulse of digitization, POD, is defined to be the individual pulse
 360 recorded by DAQ system in only one PMT channel. Two steps are done for this processing: (1)
 361 waveform reconstruction, and (2) pulse shape characterization.

362 The waveform is reconstructed with the following method. First, the baseline voltage of the pulse
 363 (RQ name: ‘baselines’) is found from the average DC voltages of the pulse of the first 10 samples.
 364 The baseline voltage represents the voltage at the time when the pulse is recorded assuming no pulse
 365 occurs. Samples used for baseline finding are 80 ns ahead the trigger time of the pulse. Therefore,
 366 these samples provide a reliable measure of the baseline since they are close in time with the rest
 367 of the pulse and they are unaffected by the rest of the pulse. There are some smaller fluctuation of
 368 baseline voltages for both PMTs. The amplitude of fluctuation ~ 0.36 mV is very small comparing
 369 to SPHE pulse amplitude, which is 15 mV to 35 mV. After baseline finding, the baseline value was
 370 subtracted from the digitized data to get the waveform for the pulse. The waveform is then scaled
 371 back from ADC counts to mV to get the reconstructed waveforms. Along this process, RQs for
 372 the voltage of the trigger sample (RQ name: ‘trigvals’), the voltage of the first sample (RQ name:
 373 ‘firstvals’) are also calculated.

374 From the reconstructed waveform, the maximum positive amplitudes(RQ name: ‘waveampli-
 375 tudes’) and the pulse area (RQ name: ‘waveareas’), which is the time integral of the pulse amplitude
 376 are calculated. However, because of the long post delay duration ($2\ \mu\text{s}$, 500 sample) from the DAQ
 377 pulse recording, baseline fluctuation during the post delay era is included in the total time integral
 378 of the pulse area. This biases our understanding of pulse area. Thus, another revised pulse area RQ
 379 (RQ name: ‘waveareas_trim_end’) is calculated from integrating the waveform with removing the
 380 last $1.8\ \mu\text{s}$, 450 sample from the end of the waveform. This revised pulse area RQ is used in main
 381 analysis instead for PMT pulse area calibrations.

382 Series of pulse shaping parameters are also calculated. Time weighted integral of waveform (RQ
 383 name: ‘wtimeN’) is used to study the skew and kurtosis of the pulse. Also, time difference between
 384 the start time of the pulse and time that the 90th percentile of the pulse waveform are calculated.
 385 They are the characteristic time differences of the pulse (RQ name: aft_tXX). They are very useful

386 for understanding the pulse shape, pulse duration, and pulse center of mass. These help pulse
 387 selection and classification discussed in the following sections.

388 **Coincidence event building and coincidence pulse processing** The DAQ system records
 389 pulses in each PMT channel independently. A true electron emission pulse usually can produce
 390 enough quantity of photons to be recorded by both PMTs. RQs of coincidence pulses between two
 391 PMTs contain more useful informations for electron emission pulses. So, for each dataset we take,
 392 we do a coincidence event building and a coincidence event processing to help us separating electron
 393 emission pulses from other background events, such as dark currents in one PMT.

394 The coincidence event building is done with the following method, requiring records in both
 395 PMTs within a short period of time. The PODs are grouped in a pending searching, which is not
 396 just two but all PODs that are recorded close in time are grouped together.

397 First, a POD time subtraction is done to preserve only the useful part of the POD signal. For all
 398 single PODs, two segments of time were subtracted from the beginning and end of a POD to reduce
 399 the influence from the baseline fluctuation in the PMT. The default values for post POD subtraction
 400 and pre POD subtraction is 1800 ns (450 sample) and 0 ns (0 sample). The time subtraction preserves
 401 120 ns before the first pre threshold crossing time, and 200 ns after the last post threshold crossing
 402 time, where between the two crossing time is the signal dominant time period. Now, this beginning
 403 and ending time of the remained part of the POD is called the start (t_{start}) and the stop time (t_{stop})
 404 of the POD.

405 Second, a POD searching is performed between a certain segment of time before the start of
 406 a single POD and the same amount of time after the stop time of the POD. The value of ad-
 407 ditional segments of time looking for coincidence is coincidence window width (CWW, RQ name
 408 ‘window_width’). The value of CWW for this analysis is $1.7\ \mu s$, if not otherwise specified. If no
 409 other pulse is found in this time region, no coincidence is found for this particular single POD. If
 410 another pulse is found in this time region, we say these two pulses are connected.

411 Third, we group all connected pulses to form undividable coincidence pulse groups. A coincidence
 412 pulse group contains all pulses that are connected to any element in the group, and cannot be divided
 413 to subgroups that match the same criterion.

414 Then, we check whether the coincidence pulse group contains PODs from both PMTs. If so, we
 415 determine a coincidence event building is successful.

416 Last, we characterize coincidence pulse RQs from forming coincidence pulse waveforms. A co-
 417 incidence pulse waveform is defined as the addition of normalized pulse waveforms in each channel.
 418 The normalization is done by dividing the pulse waveform amplitude by the SPHE pulse area in
 419 that channel. A similar pulse characterization is performed for the coincidence pulses as in single
 420 POD processing.

421 Coincidence pulse RQs are the fundamental parameters for electron emission pulse analysis frame-
 422 work, which will be described later. Some commonly used coincidence pulse RQs are listed below.

423 They are

- 424 • coincidence pulse area: RQ name ‘coin_pulse_areas_norm’, pulse area of coincidence pulse, measured in phe.
- 425
- 426 • t_{XX} : RQ name ‘coin_pulse_areas_tXX’, time difference between the start of the coincidence pulse and integrated pulse area reach XX % of the total coincidence pulse area, measured in ns. XX = 01, 05, 10, 15, 25, 50, 75, 85, 90, 95, 99.
- 427
- 428
- 429 • t_{0199} : $t_{99} - t_{01}$, also is noted as pulse duration.
- 430
- 431 • t_{1090} : $t_{90} - t_{10}$, also is noted as reduced pulse duration.
- 432
- 433 • t_{2575} : $t_{75} - t_{25}$
- 434
- 435 • section 1 area: RQ name ‘coin_pulse_areas_section1’, coincidence pulse area in the first 300 ns from the start time of the coincidence pulse, measured in phe.
- 436
- 437 • section 2 area: RQ name ‘coin_pulse_areas_section2’, coincidence pulse area in the first 800 ns from the start time of the coincidence pulse, measured in phe.
- 438
- 439 • TBA: top bottom asymmetry, $TBA \equiv (T-B)/(T+B)$, where T is the pulse area in the top PMT and B is the pulse area in the bottom PMT.

440 **Random segment sampling** The event rates are checked by looking at pulses around a random sample of times during the operation. In each dataset, 10,000 random times are chosen. From each random time, total pulse area in the preceding and the succeeding 10 μ s, 20 μ s, 50 μ s, and 100 μ s windows are calculated. These values of random sampling represent the average photon density in the detector in this dataset. They are compared to other segments of time of interest to study correlation light productions.

441 1.5 PMT Calibration

442 PMT calibrations are performed for understanding the trigger efficiency, pulse amplitude, and pulse area of a SPHE for each PMT. SPHE trigger efficiencies of a PMT, the probability of SPHE signal recording, determines the event recording efficiencies. SPHE pulse amplitude of a PMT determines the capability of DAQ to record the full height of a sized pulse. SPHE pulse area of a PMT is the fraction denominator we use to calculate the counts of photon electrons in each pulse. Counts of photoelectrons in each pulse are roughly estimated by,

$$\# \text{ photoelectrons in a pulse [phe]} \sim \frac{\text{total pulse area}}{\text{single photon electron pulse area}} \quad (1.2)$$

451 Datasets that are used in the calibration are taken at vacuum and operation voltages V_T and V_B at
 452 0 kV. The detector in this condition will have the minimum influence from events from internal and
 453 external sources. Thus, a cleaner population of SPHE can be selected.

454 **PMT trigger efficiency** PMT trigger efficiency is estimated by comparing its trigger voltage
 455 (pre threshold voltage) to its SPHE amplitude distribution. A simple Gaussian distribution is used
 456 to represent the distribution of SPHE amplitude. A fit range in the pulse amplitude of is chosen to
 457 avoid the influence from noise and overlapping of multiple photo electrons. The fit range is 12 mV to
 458 28 mV for the top PMT, and 22 mV to 38 mV for the bottom PMT. The range choices are $\sim \pm 8$ mV
 459 from the center peak values of the SPHE pulse amplitude. The trigger voltage of each PMT is
 460 compared to the survival function (complementary cumulative distribution function) of the fitted
 461 Gaussian distribution to get the trigger efficiency. Results of curve fittings are shown in Fig. 1.6.
 462 The figures show a close to unity trigger efficiency of both PMTs.

463 **PMT SPHE pulse area** PMT SPHE pulse area is calibrated with fitting the pulse amplitude
 464 and integrated area to a two dimensional Gaussian distribution. A fit range in the pulse amplitude
 465 and area is chosen to avoid the influence from noise and overlapping of multiple photo electrons
 466 this time. The fit ranges are 12 mV to 28 mV, 0 mV ns to 800 mV ns for the top PMT, and 22 mV to
 467 38 mV, 0 mV ns to 1000 mV ns for the bottom PMT. These chosen ranges contain the SPHE peaks of
 468 particular PMTs which is identified as the brightest feature above the noise and attributed to dark
 469 current. The used fitting function is,

$$z = A \exp \left(- \left(\frac{1}{2\sigma_x^2} ((x - \mu_x) \cos \theta - (y - \mu_y) \sin \theta)^2 + \frac{1}{2\sigma_y^2} ((x - \mu_x) \sin \theta + (y - \mu_y) \cos \theta)^2 \right) \right) \quad (1.3)$$

470 where x is the pulse area;

471 y is the pulse amplitude;

472 z is the total counts at each pulse area and amplitude, represented in the color scale;

473 A is the amplitude of the fit;

474 μ_x is the position of the center of the peak on x axis;

475 σ_x is the standard deviation on rotated x axis;

476 μ_y is the position of the center of the peak on y axis;

477 σ_y is the standard deviation on rotated y axis;

478 and θ is the rotated angle.

479 The mean values for pulse area and pulse amplitude are μ_x and μ_y . The standard deviation
 480 values for pulse area and pulse amplitude are $\sigma_x \cos \theta - \sigma_y \sin \theta$ and $\sigma_x \sin \theta + \sigma_y \cos \theta$. Results
 481 of these fits are shown in Fig. 1.7. Results from PMT calibrations are summarized in Table. 1.4.

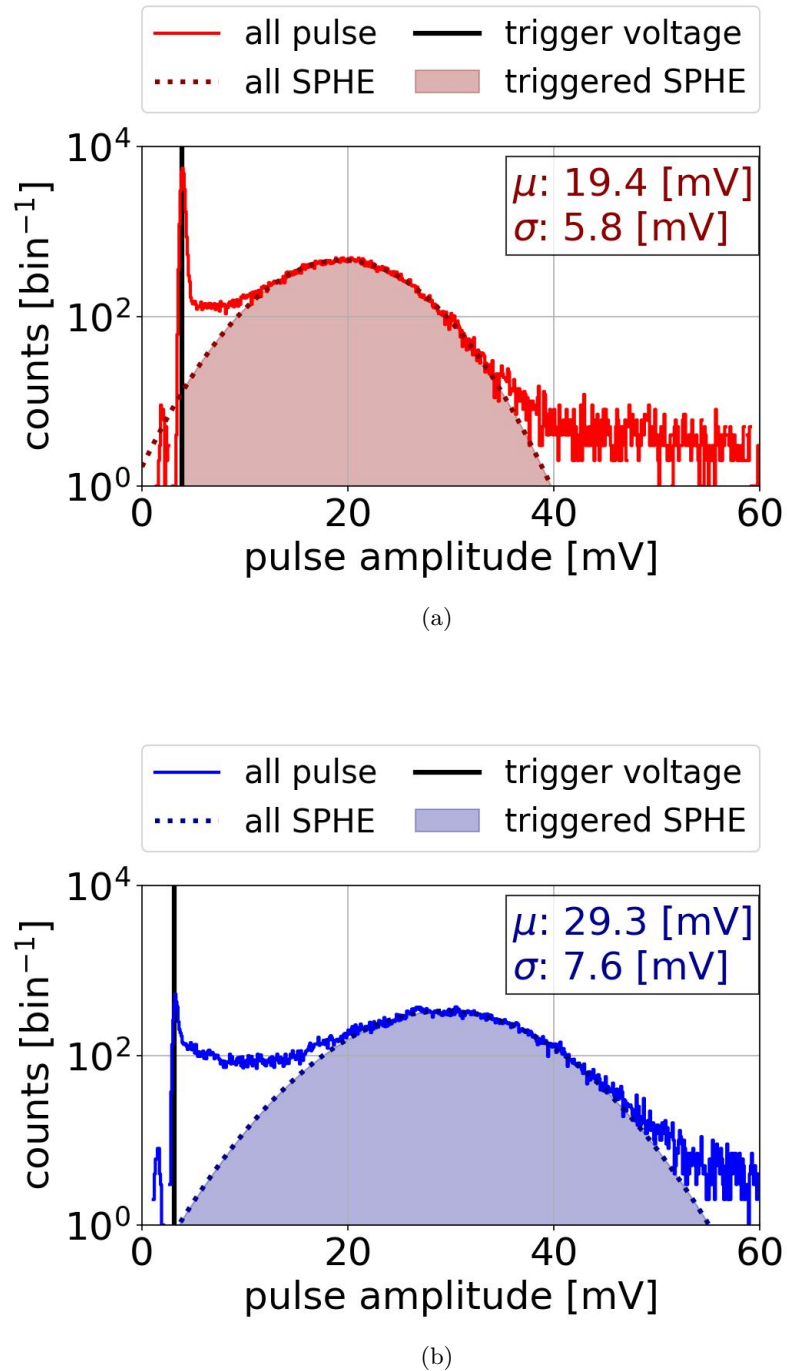


Figure 1.6: PMT pulse amplitude distribution: (a) top PMT (b) bottom PMT. Data were taken at 2018-03-12 11:41.

482 Fitting values of different dataset show an agreement within 1% on the mean PMT single photon
 483 electron pulse area and pulse amplitude.

484 The values of SPHE pulse amplitudes are approximately 20 mV for the top PMT and 30 mV for
 485 the bottom. Thus, a naive estimation based on the dynamic range noted previously shows the DAQ
 486 system allows approximately 60 SPHEs to be simultaneously recorded by the top PMT without
 487 distortion of pulse shape. The number of this is 40 for the bottom PMT. This dynamic range is
 488 large enough for record electron emission pulse without pulse shape distortion in most situations.

489 Degrading of PMTs is not noticed during the run. Technical details for the cause of degrading
 490 of PMTs are discussed in Ref. [4]. However, since this effect is not observed during the tests. For
 491 consistency of studying, the same value for PMT SPHE pulse area is used through all the studies.

492 There are two revisions of these values of SPHE pulse area. In revision 1 (Rev1), the values
 493 used are 426 mV ns for the top PMT and 638 mV ns for the bottom PMT. This is from analyzing
 494 pulse area on datasets taken with the detector filled with xenon gas and operation voltages V_T and
 495 V_B higher than 0 kV. These datasets contains more multiple photon electron pulses and biased the
 496 estimation. In revision 2 (Rev2), data taken at vacuum condition with operation voltages V_T and
 497 V_B at 0 kV are used. The values used are 413 mV ns for the top PMT and 610 mV ns for the bottom
 498 PMT. Rev2 gives a better estimation on SPHE pulse area. SPHE pulse area is noted as PHE below.

time	PMT name	trigger voltage [mV]	trigger efficiency	pulse amplitude [mV]	pulse area [mV ns]
2018-02-3 13:21	top	3.762	0.997	19.4 ± 3.3	413 ± 132
	bottom	3.103	1.000	27.9 ± 4.6	607 ± 161
2018-03-12 11:41	top	3.853	0.996	19.3 ± 3.5	411 ± 130
	bottom	3.130	1.000	29.2 ± 5.1	607 ± 161
2018-05-15 12:03	top	3.713	0.997	19.4 ± 3.5	413 ± 131
	bottom	3.091	1.000	29.5 ± 5.4	615 ± 167
adopted value (Rev1)	top	-	1	-	426
	bottom	-	1	-	638
adopted value (Rev2)	top	-	1	-	413
	bottom	-	1	-	610

Table 1.4: PMT SPHE calibration.

499 1.6 Light Collection

500 *Gas Test* studies event-based primary scintillation light and EL light. Light collection efficiency is
 501 important to understand the overall sensitivity of the detector.

$$\text{light collection efficiency} = \frac{\# \text{ photoelectrons seen by PMTs in an event}}{\# \text{ photon created during an event}} \quad (1.4)$$

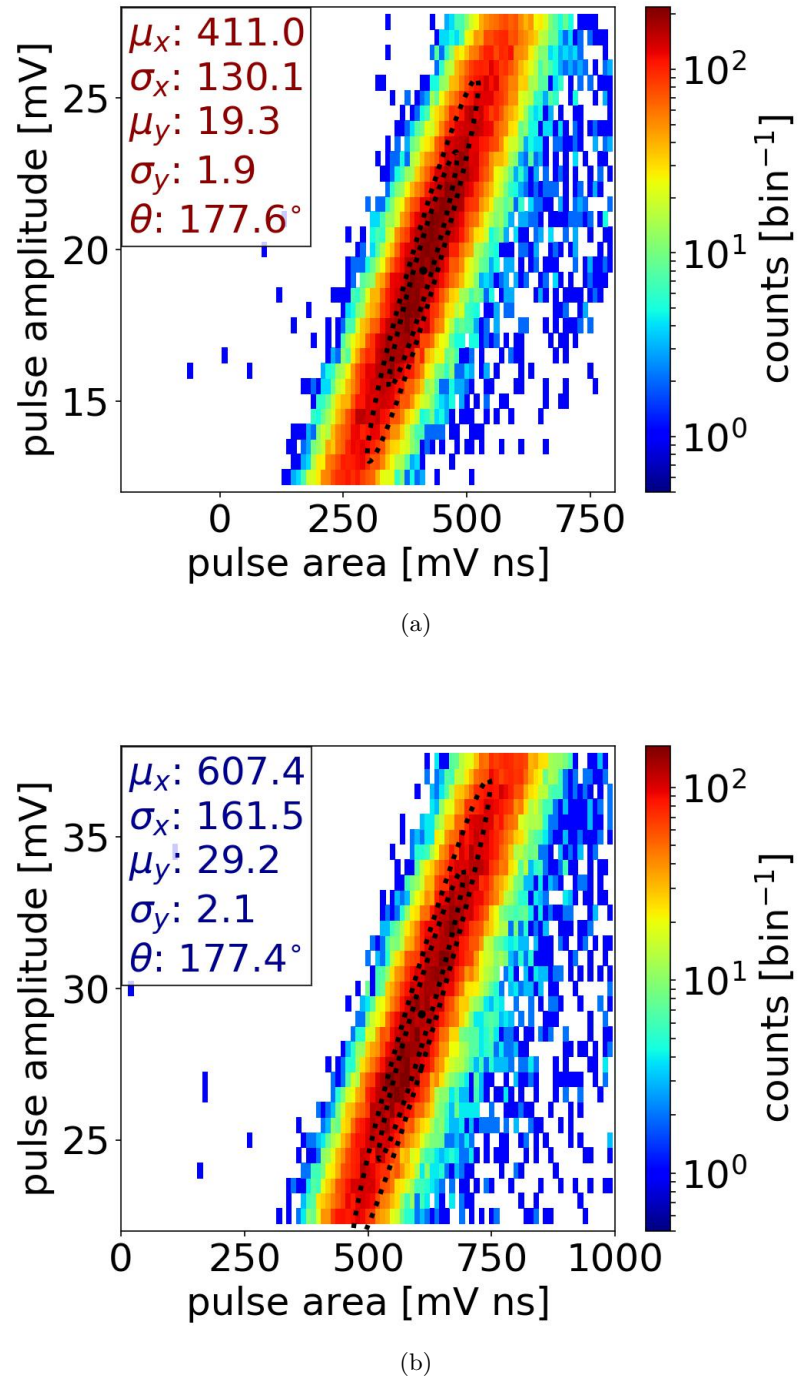


Figure 1.7: PMT SPHE pulse amplitude vs pulse area distribution: (a) top PMT (b) bottom PMT. Black dot, and dashed line are mean, 68 %, and 95 % contours of the Gaussian fits. Data were taken at 2018-03-12 11:41.

502 Light collection efficiency includes geometric collection efficiency and PMT response. Geometric
 503 collection efficiency describes the efficiency of the photon propagation in gas media, photon reflection
 504 by the detector material surfaces, and photon propagation in PMT window materials to get to PMT
 505 photocathode surfaces. PMT response describes the efficiency of how many photons are absorbed
 506 by the photocathode surfaces and turn into measurable current or voltage signals.

507 **Geometric collection efficiency** Geometric collection efficiency is studied by photon propagation
 508 simulation software Light Guide, as described in Ref. [5]. In the simulation software, a simplified
 509 *Gas Test* detector geometry boundary with cylindrical symmetry is drawn to represent the real de-
 510 tector material surfaces that reflect and absorb photons. This simplified geometry includes the
 511 photocathode surface of PMTs, inner surface of the PTFE cones, and surfaces of the grid rings.
 512 Grid wire surfaces are represents by two planes of parallel wires with the same diameter and the
 513 same pitch distance as in the real detector. The two planes are parallel to each other and close in
 514 distance to represent two distinct sets of wires interlacing each other. The empty space inside the
 515 simplified detector geometry is filled with transparent or translucent media. This software simulates
 516 photon propagation in transparent or translucent media using the physics quantity scattering and
 517 absorption of the media.

518 To understand geometric collection efficiency at one specific location in a cylindrical coordinate
 519 system, (r, z) , 10^5 to 10^7 simulations of single photons are generated from this specific location.
 520 Each simulated photon is stepped either to transport through detector media or to interact with
 521 detector surface materials. Each simulation ends when the simulated photon is absorb by either
 522 detector media or detector surface materials. Among all detector surfaces, the counts of photons
 523 reaching PMT photocathode surfaces are used to estimate geometric collection efficiency,

$$\text{Geometric collection efficiency} = \frac{\# \text{ photons reaching PMT photocathode surfaces}}{\# \text{ photons simulated}} \quad (1.5)$$

524 **PMT response** PMT response includes (1) PMT quantum efficiency (Q.E.), (2) PMT electron
 525 collection efficiency ,and (3) PMT electron gain.

526 PMT Q.E. is the ratio of output photoelectrons to incident photons. It is the efficiency of
 527 photoelectric effect including the probability of photoelectric effect creating multiple photoelectrons
 528 from a single photon (double photoelectrons effect). We use counts of photoelectrons detected (PHD)
 529 to describe the counts of photons detected without the influence of double photoelectrons effect, and
 530 counts PHE to describe the counts of photons detected with the influence of double photoelectrons
 531 effect. Statistical average one PHD is approximately 1.2 PHE. PHE is the unit that is used in this
 532 analysis. In this simulation, values of PMT Q.E. at 175 nm are used. They are 36.3 % for the top
 533 PMT and 36.0 % for the bottom PMT, see Table. 1.1.

534 PMT electron collection efficiency is the probability that these output photoelectrons land on the
 535 effective area of the first dynode. This makes the electrons go to the next dynode and being multiplied

536 by the chains of dynodes. PMT electron collection efficiency depends on PMT mechanical design
 537 and the voltage difference between the PMT photocathode and the first dynode. The exact electron
 538 collection efficiency of the PMTs used in *Gas Test* at their operation voltage are not measured. We
 539 estimate PMT electron collection efficiencies to be 90 % based on measurement of other PMTs of
 540 the same model at a higher PMT operation voltage, as described in Ref. Lung2012 .

541 PMT electron gain describes the multiplication process of the electron in dynode stages. The
 542 voltage that results from that multiplication is the measured PMT signal. The multiplication of
 543 electrons amplifies the useful signal and eases the signal noise selection. The mean value of the time
 544 integrated voltage is mean pulse area in PMT calibration. The coefficient of variation (CV, the
 545 ratio of the standard deviation to the mean value) for mean pulse area is $\sim 30\%$, as described in
 546 Section. 1.5.

547 So, for understanding the spacial dependence of the light collection in the ELD, we start with
 548 500 000 simulations of single photons every 5 mm in r and z dimension in the ELD, and record the
 549 geometric collection efficiency of each location. This number is then multiplied by PMT Q.E. and
 550 PMT electron collection efficiency to get the total light collection efficiency. We estimated light
 551 collection efficiencies of two different grid wire configurations that we used for grid emission tests.
 552 Run 4 to 9 use configuration 1, and Run 10 to 17 use configuration 2. These two configurations are
 553 identical everywhere in the ELD except for the top and bottom grid wire pitches and diameters.
 554 Table. 1.5 and Table. 1.6 summarize the parameters in the simulation.

parameter		Config 1 Run 4-9	Config 2 Run 10-17
top grid	wire pitch [mm]	2.5	5
	wire diameter [μm]	100	150
bottom grid	wire pitch [mm]	2.5	same
	wire diameter [μm]	75	same
top/bottom cone (PTFE reflector)	cylinder 1 height [mm]	1.17	same
	cylinder 1 radius (frustum larger radius) [mm]	65	same
	frustum height [mm]	98.8	same
	cylinder 2 radius (frustum smaller radius) [mm]	32	same
	cylinder 2 height [mm]	10	same
top/bottom PMT	photocathode radius [mm]	32	same

Table 1.5: Light collection simulation geometry parameters

555 As expected, the geometric collection efficiency varies at different locations in the ELD, which
 556 causes the light collection efficiency to vary, accordingly. The difference between top PMT collection
 557 efficiency and bottom PMT light collection efficiency also varies across the ELD. This difference
 558 helps discriminate the location where events happened. We use top bottom asymmetry (TBA) to
 559 describe this difference.

	parameter	value
Xe (gas)	refraction index	1.544
	Rayleigh scatter length [m]	500
	absorption length [m]	500
Quartz (synthetic quartz)	refraction index	1.000702
PTFE	reflectivity	0.4 (0-1.0) (Ref. ??)
	specular reflection ratio	0
	Lambret diffusion reflection ratio	1
SS (SS304)	reflectivity	0.18 (Ref. ??)
	specular reflection ratio	1
	Lambret diffusion reflection ratio	0

Table 1.6: Light collection simulation material parameters

$$\text{TBA} = \frac{\text{Top PMT light collection} - \text{Bottom PMT light collection}}{\text{Top PMT light collection} + \text{Bottom PMT light collection}} \quad (1.6)$$

560 Results in Fig. 1.8 show the light collection efficiency and the TBA in the ELD. Locations that
 561 are in the top cone region get a larger than zero TBA, and locations that are in the bottom cone
 562 get a smaller than zero TBA. TBA is close to zero in the EL region.

563 Among all different classes of events, our primary pulse of interest is electron emission pulse,
 564 which happens in the EL region. We estimate the light collection in this region with the same
 565 method mentioned before and finer binning. We start with 500 000 simulations of single photons
 566 every 4 mm in r dimension in the middle of the EL region. Results of the simulations are shown
 567 in Fig. 1.9. Light collection efficiency in the EL region falls away at $r \gtrsim 65$ mm, which is the inner
 568 radius of the PTFE reflector cones. The average top and bottom PMT light collection efficiencies in
 569 the EL region are ~ 0.0085 . The average TBA in the EL region is ~ 0 . The average total PMT light
 570 collection efficiency in the EL region is ~ 0.017 . This light collection efficiency allow us to detect
 571 electron emission events.

572 The change of PTFE reflectivity has a big influence on the total PMT light collection. The
 573 reported measured values of PTFE reflectivity of xenon scintillation photons in room temperature
 574 are in range 0.4 to 0.75. This difference in reflectivity may be a result of different synthetic processes
 575 or different material density, as discussed in Ref. ???. The influence on the total PMT light collection
 576 is shown in Fig. 1.10. Higher PTFE reflectivity results a higher total light collection efficiency. The
 577 actual value of reflectivity of the PTFE reflector cones is not measured directly. We estimate the
 578 actual PTFE reflectivity of xenon scintillation photons to be 0.4, according to the material density .

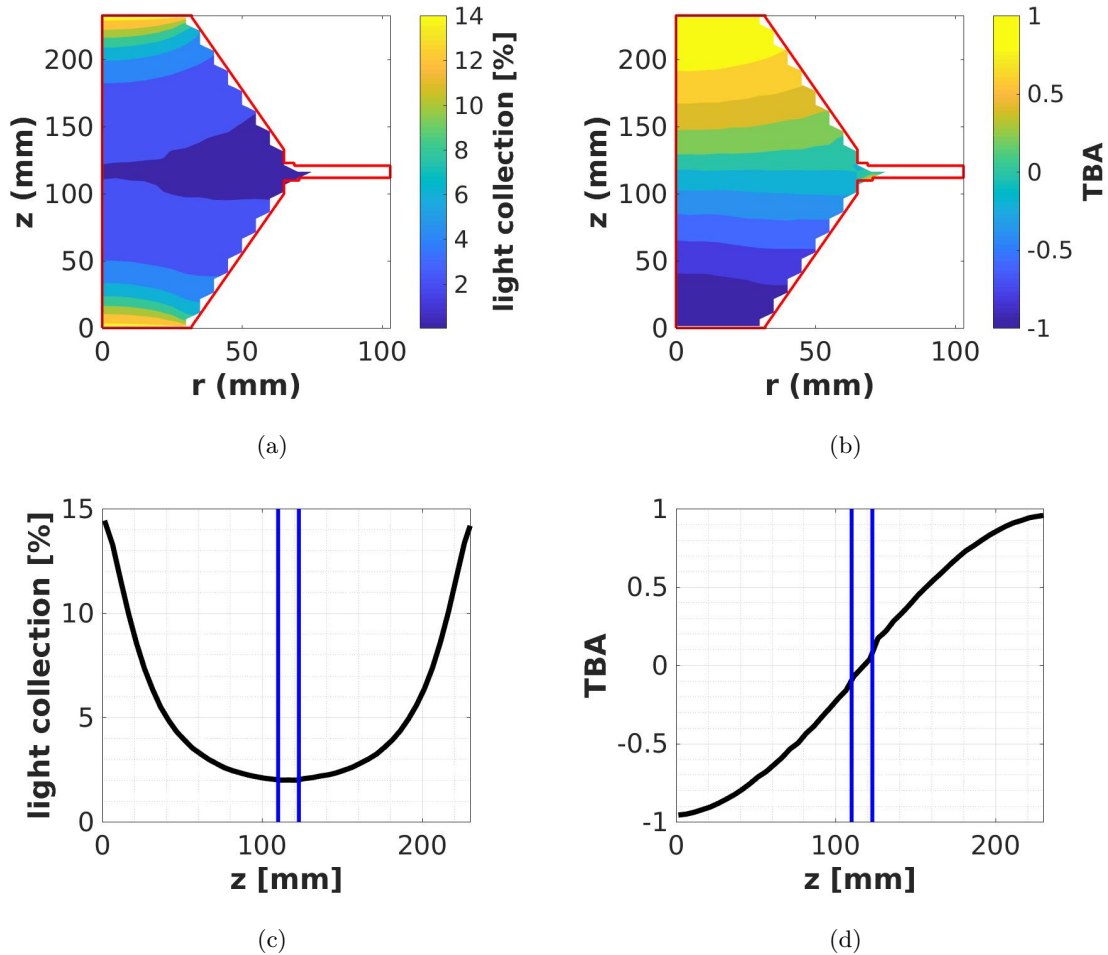


Figure 1.8: Light collection efficiency of rz cross section in the EL region. (a) total light collection efficiency (b) TBA. (c) total light collection efficiency at $r=0$. (d) TBA at $r=0$. The red solid curve is the edge of the ELD. The blue solid curve is the edges of the EL region. This result uses configuration 1, PTFE reflectivity 0.40. $z=0$ is at bottom PMT photocathode surface.

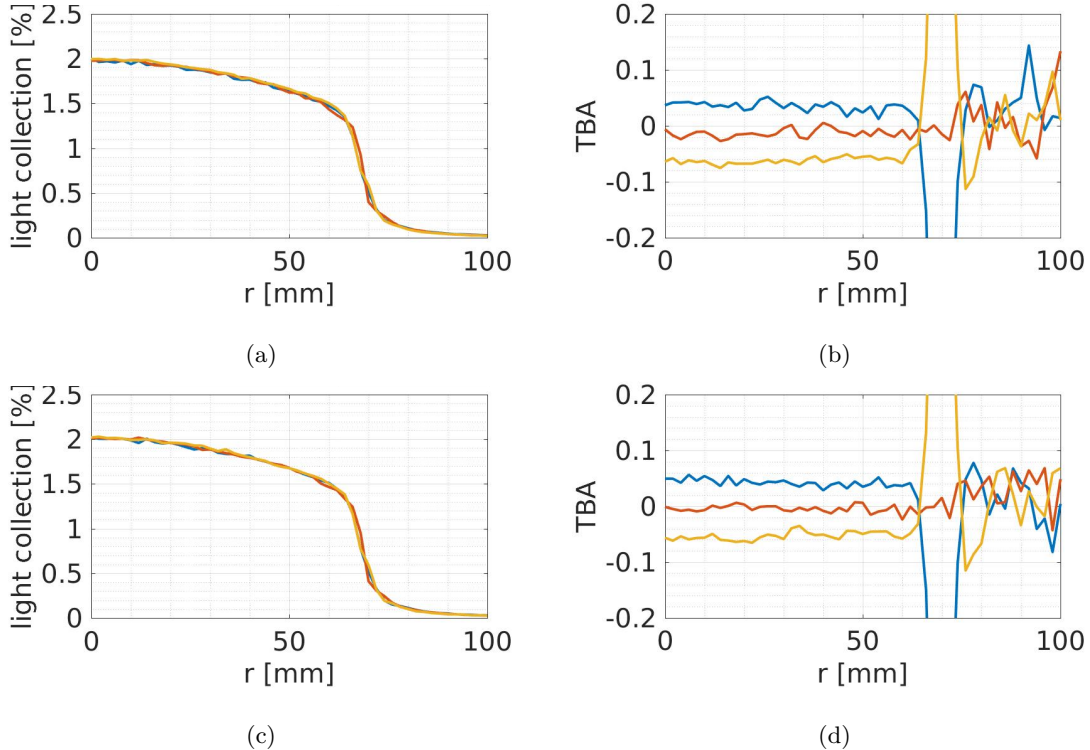


Figure 1.9: Light collection efficiency in the EL region with different configuration. (a) total light collection efficiency in configuration 1. (b) total light collection efficiency in configuration 2. (c) TBA in configuration 1. (d) TBA in configuration 2. The blue solid curve is 2 mm below the top grid. The yellow solid curve is 2 mm above the bottom grid. The red solid curve is in the middle between the top and bottom grids. This result uses PTFE reflectivity 0.40.

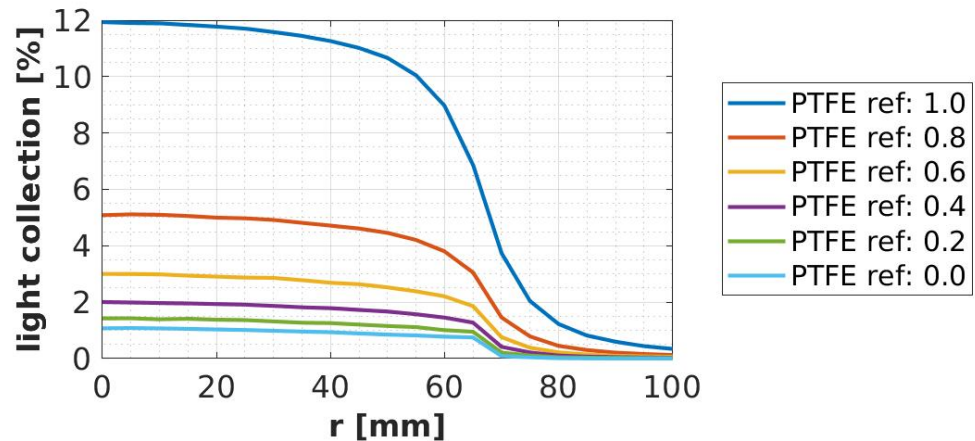


Figure 1.10: Light collection efficiency in the EL region with different PTFE reflectivity. This result uses configuration 1.

579 1.7 Light production

580 The ELD measures primary scintillation photons and electroluminescence photons. So, first I will
581 introduce these two light production processes. Then, I will discuss about the light production in
582 noble gas, e.g. xenon, which is the medium that the ELD normally operates in.

583 **Primary scintillation** Primary scintillation is the process that photons are created directly by
584 energy deposition of external particle events. These photons have two sources: direct excitation,
585 and excitation from recombination after ionization. An external particle travels through the media
586 in the ELD, transferring its energy to atoms/molecules in the media through exciting and ionizing
587 these atoms/molecules. The excited atoms/molecules will deexcite to their ground states by
588 emitting photons of series energies corresponding to the energy level of the atoms/molecules. These
589 photons from direct excitation from external particles are the first source of primary scintillation
590 photons. The ionized atoms/molecules are not able to produce photons by themselves. However,
591 they can recombine with the electrons around them and form excited atoms/molecule. These excited
592 atoms/molecules deexcite in a similar process as direct excited atoms/molecules, and emit photons
593 simultaneously. These photons are the second source of primary scintillation photons. From the de-
594 scription of the process, the quantity of second source of primary scintillation photons is dependent
595 on the recombination between ionized atoms/molecules and electron. The recombination process
596 is dependent on properties of the atoms/molecules, and influenced by the detector environment,
597 especially the electric field (or reduced electric field) on the recombination site. A strong electric
598 field allows electrons to quickly drift away from the ionization site and reduce the probability of
599 recombination, thus reduce the quantity of primary scintillation light production.

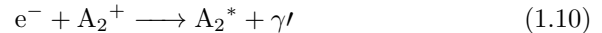
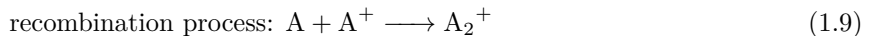
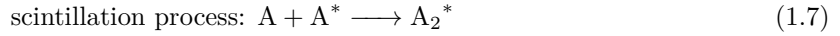
600 **Electroluminescence** Electroluminescence(EL) is a phenomenon that when an electron drifts
601 through a strong electric field in a medium, it collides with atoms in the medium, excites them which
602 will afterwards emit scintillation light. Since, EL process is related to electrons in the media, we
603 measure EL photons to know the electron production in the detector. The mechanism of EL is similar
604 to primary scintillation, which is a result from that the electron gains energy from drifting through
605 the strong electric field and simultaneously loses energy though exciting and ionizing medium atoms.
606 Moreover, the ionization process are associated with electron multiplication (gas gain), which creates
607 more electrons in the strong electric field region which are able to produce more EL scintillation light.
608 The quantity of EL scintillation photons and the probability of electron multiplication, are related
609 to the strength of reduced electric field of the media. With proper strength of reduced electric field,
610 EL can produce more photons than primary scintillation. Because of its association with electrons
611 and its production quantity, EL photons are the most important signals measured in the ELD.

612 The primary scintillation photons are called S1, and the EL scintillation photons are called S2,
613 because the primary scintillation photons are produced earlier than the other photons created by

614 electroluminescence process of uncombined electrons. The same concepts of primary scintillation,
 615 as well as S1, S2, are also used in liquid noble detectors, as described in Chapter. ??.

616 **Noble gas scintillation** For most noble gas atoms (A), e.g. neon, argon, krypton, and xenon, the
 617 scintillation process usually forms a intermediate excited excimer state (A_2^*). The emitted photons
 618 from the intermediate excimer state are almost monoenergetic, 7.1 eV (~ 175 nm), and transparent
 619 to the media. Because of the existence of the intermediated excited excimer states, it creates
 620 appreciable quantity of monoenergetic photons from the excitation of these states. These features
 621 allow us to efficiently collect these monoenergetic photons with designed devices, e.g. PMTs, and
 622 use these photons to study reactions between external particles and media atoms.

623 The chemical processes of scintillation are:



624 where γ is the monoenergetic photons from deexcitation of the excimers, and γ' is photons of other
 625 energy.

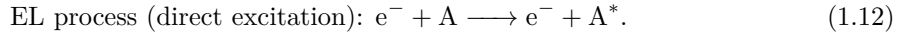
626 Both scintillation and recombination processes end up with deexcitation of excimers. The re-
 627 combination process turn ions into excited atoms and excimers, which will deexcite similar as the
 628 scintillation process. The quantity of the monoenergetic photons is related to the reaction energy
 629 between external particles and media atoms, and properties and physical environment of the media
 630 (especially media density and electric field).

631 These two primary scintillation processes happen fast in xenon, dominated by the excimers decay
 632 time. The excimers can be separated to two types, the singlet state (${}^1\sigma_u^+$, ${}^1\Pi_u$) and triplet state
 633 (${}^3\sigma_u^+$, ${}^3\Pi_u$), with separate decay times. The singlet state and the triplet state are known to be
 634 created from a three-body deconstruction of noble gas atom excited state ${}^2P_{1/2}$ state and ${}^2P_{3/2}$
 635 state, which has a different initial quantity from the event. Because these creation processes are
 636 three body reactions, the creation rate of the these two states have strong dependence on the gas
 637 density of atoms. The decay time of both of these two states have a dependence on the gas density,
 638 as described in Ref. [6]. Some other materials also show that the decay time is very different between
 639 liquid noble gas and very dense noble gas. The decay time for the singlet state and the triplet state
 640 in liquid xenon are 4.3(6) ns and 22.0(20) ns, as measured in Ref. [7]. For dense xenon with pressure

641 in range 2.7 atm to 32 atm, the decay time for singlet states varies from 15(3) ns to 5.5(10) ns. The
 642 decay time for triplet state is 96(5) ns in the same pressure range.

643 **think about should I take about ionization/scintillation ratio here?**

644 EL photons in xenon are the predominant signals we measure. These photons are predominantly
 645 created by direct excitation in gaseous xenon is . The chemical process is,



646 The EL reduce photon production quantity (ratio of photon production quantity to gas density) per
 647 electron trajectory length of direct excitation is found to have a linear dependence on the reduced
 648 electric field (E_s/N), as described and summarized in Ref. [8–11]:

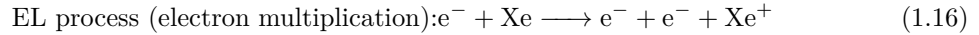
$$\frac{dL_s}{dx} = a \frac{E_s}{N} + b, \quad (1.13)$$

649 where L_s is the reduced photon production quantity; x is the electron trajectory length; E_s is
 650 the electric field strength (at the scintillation site); N is the density of gas; a and b are constant
 651 parameters, which are measured in Ref. [11] to be:

$$a = 0.137(2) \text{ phe eV}^{-1}, \quad (1.14)$$

$$b = -4.7(1) \times 10^{-18} \text{ phe cm}^2 \text{ electron}^{-1} \text{ atom}^{-1}. \quad (1.15)$$

652 An EL process is usually associated with simultaneous electron multiplication. This process
 653 describes an electron accelerated by electric field, collides with gas molecules, ionize them generating
 654 additional free electrons. The chemical process is,



655 The probability of electron multiplication per electron per unit length is also quoted as the first
 656 Townsend ionization coefficient (α), which depends on the strength of reduced electric field, as mea-
 657 sured in Ref. [Kruithof1940, Derenzo1974]. Conventionally, reduced first Townsend ionization
 658 coefficient is measured with E/p_0 instead of reduced electric field, where E is the electric field; p_0 is
 659 pressure of the gas reduced to 0 °C. The reduced first Townsend ionization coefficient $\eta \equiv \alpha/E$ is also
 660 frequently used. The measured reduced first Townsend ionization coefficient is shown in Fig. 1.11.

661 The duration of EL process is related electron drift velocity (v), which also depends on reduced
 662 electric field (E/n), as measured in Ref. [12–16]. In range 5 Td to 25 Td, a naive linear fit from
 663 Ref.[15] shows in xenon,

$$v[\text{mm } \mu\text{s}^{-1}] \approx 0.56E/n[\text{Td}] \quad (1.17)$$

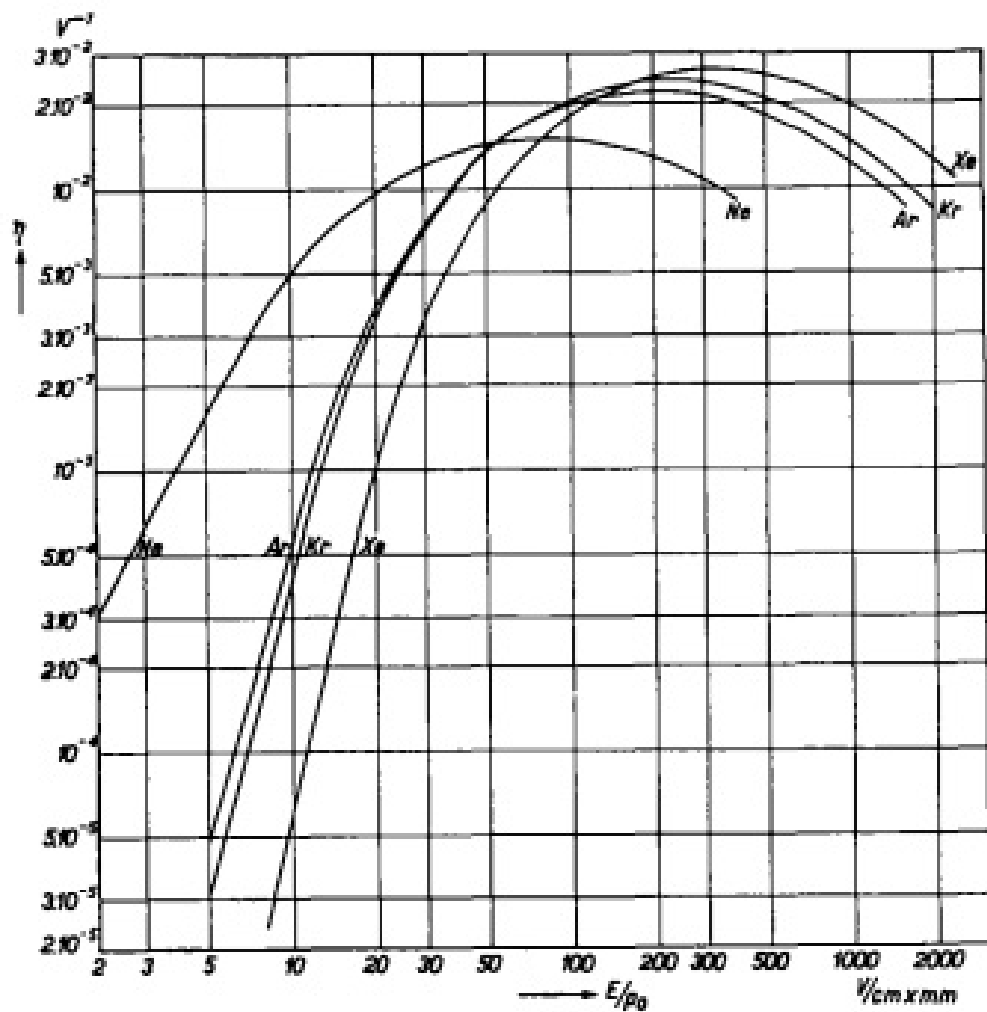


Figure 1.11: The reduced first Townsend ionization coefficient $\eta \equiv \alpha/E$ for neon, argon, krypton, and xenon, from Ref. [Kruithof1940].

664 Therefore, xenon is a good scintillation medium for its quantity of photon production and its
 665 transparency to these photons. With its well characterized quantities, we chose it as the major
 666 operation medium for the ELD.

667 1.8 Events

668 **Electron emission** A cartoon for the physical process and an example waveform of electron
 669 emission pulse are shown in Fig. ???. An electron leaves the cathodic electrode from various types
 670 of emission processes. After the electron left the wire surface, the high electric field around the
 671 cathodic wire will quickly energize the electrons. The high energy electron ionizes and excites the
 672 atoms around it and create more electrons. In this region, more EL light is produced per second
 673 comparing to a lower electric field region. This is the cause of the “peak” at the beginning of the
 674 electron emission pulse. This process is called electron multiplication. Then, these electrons drift
 675 to the anodic electrode due to the operation voltage difference between the two grids. EL light is
 676 produced along this drift. This correspond to the majority of EL light seen in the electron emission
 677 pulse. There is a clear start and stop time for the electron emission pulse. Duration of the electron
 678 emission pulse is roughly the duration of this drift. After this, electrons get close to the anodic
 679 electrode. Since the electric field around the anodic wires are also high, electrons also go through a
 680 similar electron multiplication process. This process also creates more electrons and a higher density
 681 of EL light. This is the cause of the “peak” at the ending of electron emission pulse. The peak at the
 682 end of the pulse is lower than the peak at the beginning of the pulse. This is because of dispersion of
 683 the arrival times of electrons on anodic electrode. This dispersion is due to the different microscopic
 684 trajectory each electron takes to reach the anodic electrode. Different arrival times of the electrons
 685 cause the final increment of EL light productions from different electrons do not happen coincidently.
 686 This lowers the height of the peak at the ending of the electron emission pulse. Another reason for
 687 the different height of the peak is due to the electric field on the anodic wire is smaller than cathodic
 688 wire. It also results in a smaller production of EL light.

689 Therefore, one important signature of electron emission pulse is the EL duration. EL duration
 690 is approximately equal to duration of electron drift between the two electrodes. The deviation of
 691 electric field between the two electrode is much smaller than the average value of it. So the drift
 692 duration can be roughly estimated by,

$$\text{drift duration} = \frac{\text{distance between two electrodes}}{\text{drift velocity at the average electric field between two electrodes}} \quad (1.18)$$

693 EL light production in the majority part of electron emission pulse is uniform, except for the
 694 beginning and the ending of the pulse. Since the electron multiplication around the cathodic wires
 695 happens early in the process before the major era of EL light production. The total counts of

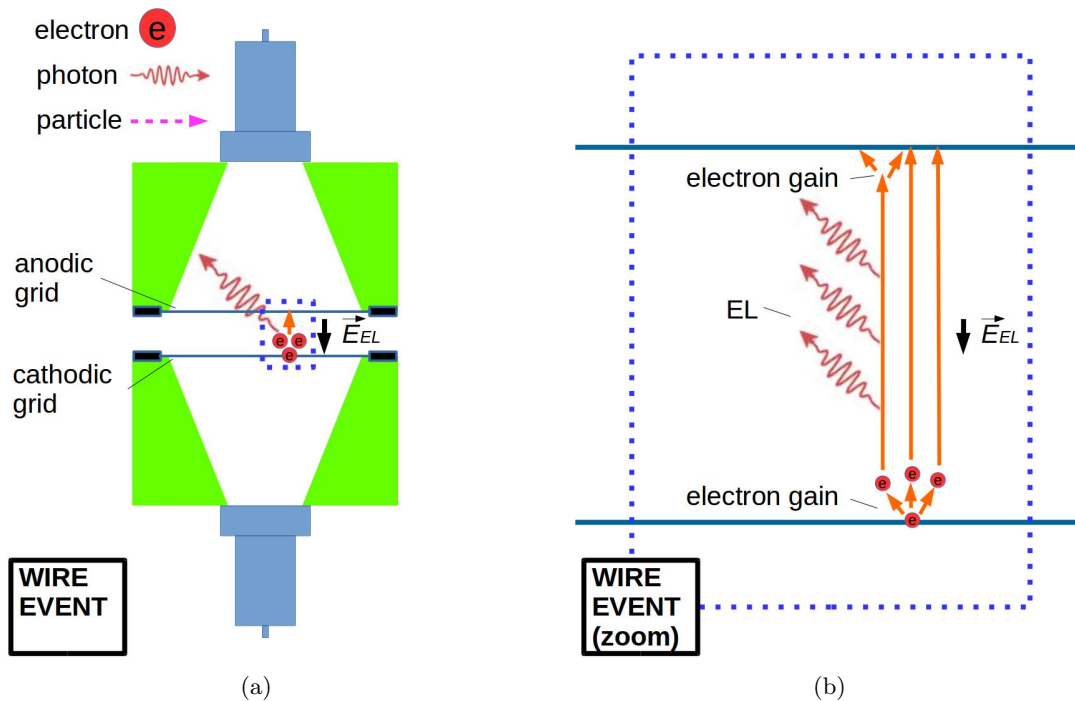


Figure 1.12: *Gas Test* electron emission event from grid wires: (a) illustration cartoon (b) illustration cartoon (zoom) (c) an example waveform.

696 photons created in an electron emission pulse can be estimated as,

$$\# \text{photons created} \approx \# \text{electrons after (cathodic) electron multiplication} \quad (1.19)$$

$$\times \# \text{EL photons production per single electron} \quad (1.20)$$

697 The counts of electrons after (cathodic) electron multiplication are related to the surface electric
 698 field on the cathodic wire. The value of the cathodic surface electric field can be estimated from the
 699 operation voltage, wire diameter and wire pitch of the two grid. The counts of EL light production
 700 per single electron are related to the distance and the electric field between the two grids. The
 701 average photon yield per EL distance is a known function of electric field. The value of the electric
 702 field between two grid can also be estimated from the operation voltage, wire diameter and wire
 703 pitch of the two grids.

704 The electric field in ELD is solved by . Appendix. ??

705 **Electron multiplication simulation** Electron multiplication is studied using gas simulation
 706 softwares. A simple geometry is build and meshed in GMSH, as described in Ref. Gmsh2011. Fig. ??
 707 shows the built geometry. This geometry includes a thin cylinder surface in the center representing
 708 the grid wire as the electron emission surface, and a thick cylinder surface outside representing the
 709 cut off distance of electron multiplication. The cut off distance is chosen to be sufficiently long so
 710 that the electric field beyond this distance is too small to allow significant electron multiplication.
 711 The diameter of the two cylinders are $75 \mu\text{m}$ and 1 cm. Voltages are assigned to two cylinders to
 712 create a chosen electric field on the surface of the wire. Then, the electric field map in this full
 713 geometry is solved by ElmerGrid, as described in Ref. Elmergrid2000. The gas simulation is done
 714 with Magboltz in Garfield interface, as described in Ref. ???. These softwares implement light yield
 715 and charge yield, aka the photon and electron productions, for electrons moving in gas medium as
 716 a function of reduced electron field. By including the electric field map, choosing the correct gas
 717 density, these softwares simulate the photon and electron productions with an electron that initiate
 718 from the wire surface.

719 An example of electron multiplication simulation in the simple geometry is shown in Fig. ???. As
 720 the electron moves further away from the wire surface, both light production and electron production
 721 reduce. Results of the counts of electron multiplication vs surface electric field at different gas density
 722 is shown in Fig. ???.

723 1.9 Cuts

724 I think I should arrange the cuts by what I think is the origin of the cuts rather than category by
 725 pulse shape and uncorrelation. think about it more.

This section discusses pulse selections, aka cuts, that are used in *Gas Test* analysis. The purpose of this analysis is searching for electron emission pulses from tested grid wires and correctly estimating the rate of this process. Pulse selections are done on different parameter spaces. For each pulse selection, possibility of removing signals of interest (in this case: electron emission pulse) is evaluated. The primary principle of pulse selections is to get a clean population distribution of electron emission pulse to get a reliable estimation of its rate. Other than that, since electron emission pulses are in most situation rare in the detector, pulse selections of these electron emission pulses are done conservatively. That is to keep as many candidates for electron emission pulses as possible.

An electron emission pulse should:

- be an uncorrelated pulse from previous pulses in time, and
- have the correct pulse shape.

To make the pulse selections, a study of the electron emission pulse is done for understanding its pulse shape. Background events that originate from different source will be separately discussed. Their pulse shape and rate are studied. The cuts that removes these backgrounds are described. Finally, the efficiencies of these cut and their potential of removing good electron emission pulse candidates are estimated. Corrections for these efficiencies in this analysis are also described in the end.

Light collection of created photons also influence the total counts and duration of electron emission pulse. The approximately 2 % light collection efficiency in the ELD results in only a portion of EL photons are seen by the PMTs. It causes the waveform of an electron emission pulse more coarsely distributed in time. This low number of collected photons also increases the difficulty of estimating the real EL duration.

Based on these knowledge, a list of detailed selections are done. These selections will be discussed below.

1.9.1 Coincidence found

Definition Both PMTs have pulses that occur with a time difference smaller than CWW.

Purpose This is to make sure that the signal of interest is unlikely to be from dark current in one PMT, afterpulsing in one PMT, dead time or misbehavior period of one PMT, or other SPHE source (ex. fluorescence light from PTFE, microscopic sparking) in one PMT. This is also to make sure the signal of interest is not from a random coincidence of previous sources in one PMT channel.

Coincidence found and coincidence pulse building are the fundamental part of this analysis. Cuts defined later are based on the classification of coincidence pulses.

⁷⁵⁹ **Method** Details are discussed in data processing section in the earlier context, see Section. 1.4.

⁷⁶⁰ 1.9.2 Uncorrelated from preceding pulses

⁷⁶¹ This cut is to make sure that the signal of interest is not in the tail of any preceding signal. Source
⁷⁶² of this type of background are: (1) an anode cone event, and (2) fluorescence photon following a
⁷⁶³ big pulse. The cuts for resolving these two backgrounds are (1) short following period veto, and (2)
⁷⁶⁴ long following period veto.

⁷⁶⁵ 1.9.2.1 Short following period veto

⁷⁶⁶ **Definition** Coincidence pulse is not following another pulse within $100\ \mu s$

⁷⁶⁷ **Purpose** This is to make sure the signal of interest is not a part of anode cone event. This is also
⁷⁶⁸ to resolve dead time of DAQ.

⁷⁶⁹ **Anode cone event** A cartoon for the physical process and an example waveform of anode cone
⁷⁷⁰ event are shown in Fig. 1.13. An external particle can enter the anode cone region and deposit energy
⁷⁷¹ there. This process excites xenon atoms in the cone region and results in generating scintillation
⁷⁷² photons and free electrons. The scintillation photons are collected and seen immediately. These
⁷⁷³ free electrons drift to the anodic grid. Electric field in the cone region is too small to produce large
⁷⁷⁴ quantity of EL light during electron drift. However, when these electrons get close to the anodic
⁷⁷⁵ grid wire, the electric field around the anodic grid wires are big enough to produce EL light. This
⁷⁷⁶ is the source of the secondary photon signal, which follows the preceding signal after the amount
⁷⁷⁷ of time that it took electron to drift. The time separation is estimated by the known measured
⁷⁷⁸ electron drift velocity in gaseous xenon, as described in Ref. ???. Electron drift velocity in gaseous
⁷⁷⁹ xenon is approximately $5.56\text{ mm}\ \mu s^{-1}\text{ Td}^{-1}$ for reduced electric field in range 5 Td to 25 Td. The
⁷⁸⁰ maximum separation time for this detector at xenon gas density 0.137 mol L^{-1} , operation voltage V_T
⁷⁸¹ in range $+4\text{ kV}$ to $+8\text{ kV}$ is approximately $85\ \mu s$ to $75\ \mu s$. The value of this maximum separation time
⁷⁸² decreases as decreasing the operation pressure in the detector. The value of maximum separation
⁷⁸³ time drives the choice of $100\ \mu s$ quiet preceding requirement.

⁷⁸⁴ This background from the secondary photon signals in anode cone events has a different pulse
⁷⁸⁵ shape from electron emission pulse. The pulse shape of the secondary photon signals has a compara-
⁷⁸⁶ rably slower rising and falling edge at the beginning and the ending of it. It also has a higher TBA.
⁷⁸⁷ This is because EL around the anode wire primarily happens above the anodic wire. The bottom
⁷⁸⁸ PMT is in the shadow of grid wires when the top PMT is not. It causes a ratio of ~ 2 increment on
⁷⁸⁹ light collection ratio between top PMT and bottom PMT. These characteristic signatures are useful
⁷⁹⁰ for veto large area anode cone events. However, when their pulse area get smaller (probably due

791 to a lower energy deposition of external particles), it becomes difficult to find these pulses by their
 792 shape. Thus, this cut is performed.

793 This cut also removes **describe the small area stuff**.

794 This cut also resolves the dead time issue, **explain here**.

795 **Method** For the start time of each coincidence pulse, a searching is done for pulses in the preceding
 796 $100\ \mu\text{s}$. If there is any pulse in any PMT, the coincidence pulse is vetoed.

797 The effect of this cut is shown in Fig.??.

798 1.9.2.2 Long following period

799 **Definition** Coincidence pulse is not following any single pulse that has pulse area larger than
 800 100 phe within 10 ms

801 **Purpose** This is to make sure the signal of interest is not following a large EL light production.
 802 An example waveform is shown in Fig. ???. Following a EL light production, PTFE will absorb the
 803 EL photons and re-emit photons not immediately. The time distribution of the after emission of
 804 photons roughly follow an exponential decay model. This effect is called PTFE luminescence. This
 805 effect is noticed in the previous literatures. Measurements of fluorescence rates and decay time τ
 806 have a various range. This might be caused by different conditions of synthesis, as described in
 807 Ref. [17]. This effect is also believed to cause the slow decay of electron signal in liquid xenon TPCs.
 808 A decay time of 2.3 ms is reported in Ref.[18]. A decay time of 10 ms is reported in internal review
 809 in LUX. The accidental coincidence of the following emission from PTFE can mimic an electron
 810 emission pulse. The rate of PTFE fluorescence is strongly dependent on the previous luminance
 811 history in the detector. Thus, this cut is performed after all large EL production in the detector.

812 **Method** For each single pulse in one PMT, if its pulse area is larger than 100 phe, the coincidence
 813 pulse happens in the following 10 ms are vetoed.

814 1.9.2.3 Further discussion on following period veto cuts

815 These two cuts previously mentioned have potential to veto good candidate electron emission pulses
 816 . Thus, survival ratio of the candidate electron emission pulses need to be estimated. The survival
 817 ratio is estimated by how much is the fraction of a careful selection of coincidence pulses survive
 818 these cuts. The careful selection of coincidence pulses also need to be uncorrelated from preceding
 819 pulses. The careful selection is the coincidence pulses in t_{2575} range 0 ns to 200 ns, pulse area range
 820 25 phe to 250 phe. This selection is a conservative selection of S1 pulses that has few contaminations
 821 from other sources. Since S1 is from the primary light production of external particle sources, this
 822 selection of pulses are uncorrelated from preceding pulses. Thus, it can be used for estimating the

survival ratio. The survival ratio is called quiet fraction(QF). For normal operation, QF is in range 0.6 to 0.9. Details of this physical sources of S1 pulses will be discussed in the following Section. ??: S1 conservative population.

1.9.3 Pulse shape

Pulse shape is one of the most important signature for electron emission pulse. It includes the aspects of pulse area, pulse duration, and time dependent pulse density.

1.9.3.1 not noise like

Definition Coincidence pulse has a positive pulse area in all PMT channels, and a higher than 0.5 positive negative amplitude ratio. This coincidence also mush have a non-zero t_{1090} .

Purpose This is to make sure the signal of interest is not an electrical noise pulse. An example waveform of electrical noise pulse is shown in Fig. ???. These electrical noises come from the grounding of the infrastructures and detector electronic devices. An electrical noise pulse has a comparable pulse negative maximum amplitude and pulse positive amplitude. Its pulse area is usually smaller and sometimes negative. An electrical noise pulse also tend to have the waveforms in two PMTs overlapping. The negative integrated pulse area usually also makes it impossible to find the pulse characteristic time differences. Thus, this cut is performed. This cut ensures all characteristic time differences to be computable. During the tests, electrical noise pulses occurs at a rate of approximately 2 Hz.

1.9.3.2 Multiple SPHE

Definition In the coincidence pulse, one of the two PMTs contains pulse that has more than one SPHE.

Purpose This is to make sure the signal of interest is not a random coincidence of dark current (or other SPHE source) between two PMTs. This random coincidence is also called false coincidence pulse. The PMTs that are used in this study have a $\sim 1\text{ kHz}$ dark current rate. CWW is $1.7\ \mu\text{s}$ in this analysis. Combination of these two values lead to a $\sim 3.4\text{ Hz}$ rate of false coincidence pulse. The SPHE source is not limited to dark current. For example, PTFE fluorescence that is discussed previously, and microscopic discharge could also be a SPHE source.

Microscopic discharge Microscopic discharges happen outside the ELD could be a potential source of SPHE background. In sparking tests, we observe discharges on the high voltage feed throughs and cables. These discharges are caused by the smoothness of the high voltage surfaces (especially metallic surfaces) are imperfect. This imperfectness microscopically creates a high field

region, and initialized a high ionization probability of the medium (especially gas medium) surrounding it and causes a discharge. The quantity of light production of this discharge are big. The quantity also has a various range. However, since these discharge activities happens outside the ELD, light collection for these activities are usually poor. So these activities may end up having one or several SPHEs in each PMTs. Thus, microscopic discharge is also a potential SPHE source.

Therefore, to reduce the misclassification from false coincidence, this cut is performed.

Method This cut is a combination with series of vetoes. Pulse area and pulse duration are used for computing these vetoes. A coincidence pulse is vetoed if the total pulse area is smaller than 2.5 phe and the pulse area in at least one of the PMTs is smaller than 1.5 phe. This choice is to compensate the $\sim 30\%$ systematic fluctuation of PMT SPHE area. A coincidence pulse is also vetoed if the pulse duration in both PMTs are “short”. The definition of “short” is a single pulse t_{2575} smaller than 80 ns, and t_{95} smaller than 320 ns. The scatter plot of t_{2575} and t_{95} is shown in Fig.??.

The effect of this is shown in Fig. ??.

1.9.3.3 not narrow

Definition The major part of the coincidence pulse is not narrow. That is coincidence pulse t_{2575} longer than 250 ns and the time difference between the earlier of the PMT trigger time and coincidence pulse t_{50} longer than 200 ns. The narrow coincidence pulses can be separated to two categories: (1) extremely narrow coincidence pulses, and (2) not extremely narrow coincidence pulse.

Purpose This is to make sure the signal of interest is not a potential (1) Cherenkov radiation event, (2) microscopic discharge event, and (3) primary scintillation light (S1) from an external particle.

Cherenkov Cherenkov radiations in PTFE material (and PMT window) are considered one of the potential sources for the extremely narrow pulses. A cartoon for the physical process and an example waveform of extremely narrow pulse are shown in Fig. 1.14. Cherenkov radiation is the photon radiation when a charged particle is traveling through a medium with its speed higher than the speed of light in this medium. The charged particle could be an external charged particle or electrons that originate from energy loss of external particle in the medium. The Cherenkov events originate from energy loss are the potential explanation for the extremely narrow pulses.

The spectrum of Cherenkov radiation is estimated by Frank–Tamm formula. A simplified approximation for Frank–Tamm formula from Ref. [19] Eqn. 14.133 shows:

$$\frac{dI(\omega)}{dx} = \frac{e^2 \omega}{c^2} \left[1 - \frac{1}{\beta^2 \epsilon(\omega)} \right] \quad (1.21)$$

where ω is the frequency of Cherenkov radiation, $I(\omega)$ is the energy intensity of frequency ω , $\epsilon(\omega)$ is the relative permittivity of the medium, and β is the speed of the charged particle. ω satisfies that $\beta^2\epsilon(\omega)$ is larger than one, so that the energy intensity is positive. The number intensity $N(\omega)$ can be derived from Eqn. 1.21

$$\frac{dN(\omega)}{dx} = \frac{\alpha}{c} \left[1 - \frac{1}{\beta^2\epsilon(\omega)} \right] \quad (1.22)$$

where $\alpha \equiv e^2/\hbar c \approx 1/137$ is the fine structure constant. The total quantities of photons (N) is the integral over frequency and distance of Eqn. 1.22.

Since PTFE is partially transparent to these photon, a portion of the Cherenkov radiation photons can be seen by the PMTs. The duration of Cherenkov event light production is the duration of charged particle energy loss process. This duration is typically very short. A 30 keV to 300 keV electron has a stop distance of $\sim 10^{-2}$ cm to 10^{-1} cm in PTFE. We take the photon wavelength is in range 160 nm to 650 nm (the spectral response range for PMT R11410-10, as described in Ref. ??), the PTFE refractive index to be approximately 2 ($\epsilon \sim 4$). N is about 150. The attenuation distance of photons is in range 1 cm to 4 cm for 30 keV to 300 keV electrons for PTFE. The light collection is in range (1.5 % to 15 %). The estimated number of photons seen by the PMTs is in range up to ~ 100 phe. This number is hard to predict precisely because of the complicated geometry of ELD. This is not a very big number but enough to be seen by the PMTs. Thus, Cherenkov is still one of the optimal explanations for the extremely narrow pulses.

One of the most convincing evidence is this population of events are seen in the detector at vacuum condition. Fig. 1.15a shows the pulse duration vs pulse area plot from a dataset with operation voltages V_T and V_B at 0 kV, operation detector gas density at vacuum. The red population seen are the selected extremely narrow pulses. Extremely narrow pulses in vacuum data consist of events that potentially come Cherenkov in PTFE. They may come from both external charged particles and energy loss of external particles. An external muon particle will go through the PTFE cones. During the traveling of the muon particle, it ionizes and radiates photon. Since muon particles are usually more energetic than other external particles like gamma radiation, the photon radiation from muon events is usually strong. This is one explanation for the hot spot at $(10^2, 10^2)$ in Fig. 1.15a. When the detector is filled with xenon gas, the muon particle can also ionize xenon gas atoms. This produces scintillation photons and increases muon events duration. It explains the reason that this hot spot disappears in xenon gas data. Details for explanations of muon events in xenon gas data are in Section. ???. The pulses with pulse area in range 0 phe to 10^2 phe and pulse duration in range 0 ns to 2×10^2 ns in Fig. 1.15a are potentially Cherenkov events from external gamma radiation loss energy in PTFE (and PMT window). The gamma radiation ionized PTFE and free electrons which can potentially emit Cherenkov light. When the detector is filled with xenon gas, the same physical source of gamma radiation applies. This explains why a similar population

918 of extremely narrow pulses exist in both vacuum data (Fig. 1.15a) and xenon gas data (Fig. ??).

919 Other than Cherenkov, microscopic discharge that for last really short amount of time could
 920 also be the source of the extremely narrow coincidence pulses, see Section. 1.9.3.2 discussion for
 921 microscopic discharge.

922 **Method** pulse area density in the 300 ns to 800 ns range is not low,

923 1.10 Evaluation

924 1.10.1 Simulations

925 Simulations for electron emission pulse is

926 Detailed discussions of the calculation of the electric field is in Appendix ??.

927 The evaluation of these cuts are estimated by simulations. Cut efficiency is used to indicate the
 928 quality of the cuts. With evaluating the ratio between the simulated electron emission pulse passing
 929 cut and the total counts of simulations, the cut efficiency is estimated as

$$\text{cut efficiency} \approx \frac{\# \text{ pulses pass cut}}{\# \text{ simulations}} \quad (1.23)$$

930 Higher cut efficiency indicates that we are capable of preserving more electron emission pulses.
 931 Cut efficiencies are evaluated with different detector operation conditions, such as gas density and
 932 grids operation voltage. Since the simulated electron emission pulse that I used to evaluate the
 933 cuts have a few discrepancies from the real electron emission pulse, the cut efficiency will be not be
 934 exactly accurate. Even though this estimate is only an approximation, the overall cut efficiencies
 935 are not wildly off.

936 1.10.2 Summary

937 To summarize the cuts that I used, to be an electron emission pulse candidate, a pulse should satisfy
 938 these conditions. It should

- 939 • contain coincidence pulse in both PMTs,
- 940 • uncorrelated from preceding pulses,
 - 941 – not have any preceding pulse in the previous 100 μs ,
 - 942 – not have any preceding large pulse in the previous 10 ms,
- 943 • have the correct pulse shape,

- 944 – not noise like,
- 945 – not have pulse heavily concentrated only in one of the PMTs,
- 946 – have longer than single PHE pulse area or positive pulse duration in at least one PMT,
- 947 – not “Cherenkov” like,
- 948 – not S1 like,
- 949 – not muon like,
- 950 – not S1 S2 like,
- 951 – t_{1090} (reduced pulse duration) matches prediction from electron drift time between the top and bottom grids,
- 952
- 953 • not saturate any PMT (this is required for analysis with condition that gas pressure higher than 1 bara).
- 954

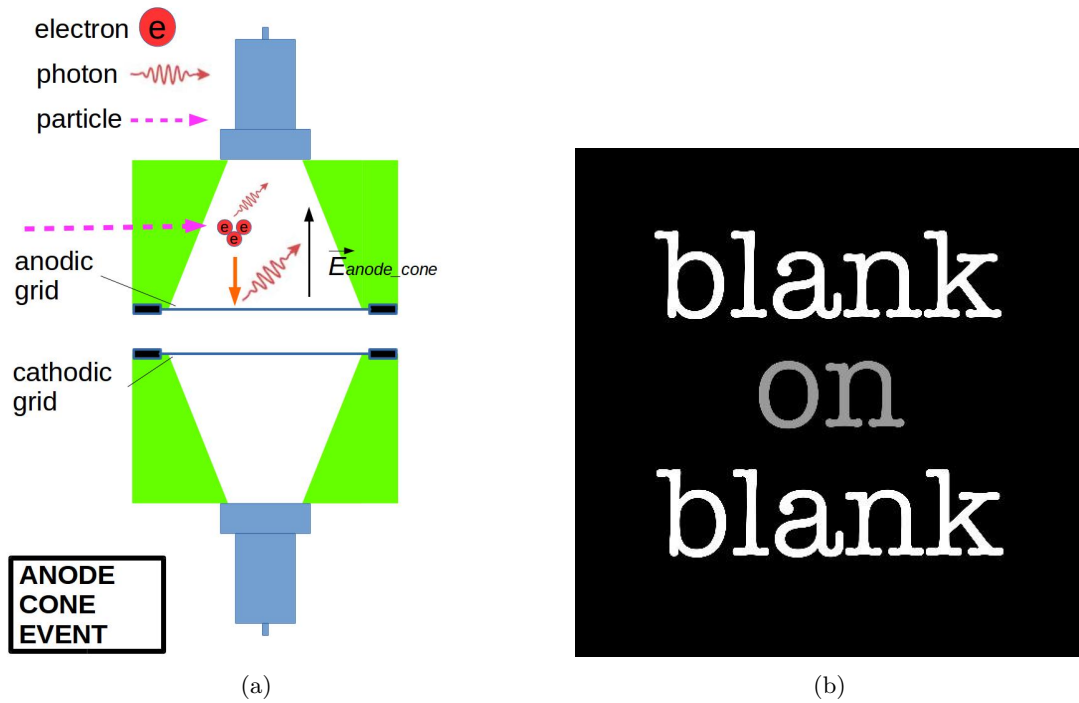


Figure 1.13: *Gas Test* anode cone event: (a) illustration cartoon (b) an example waveform.

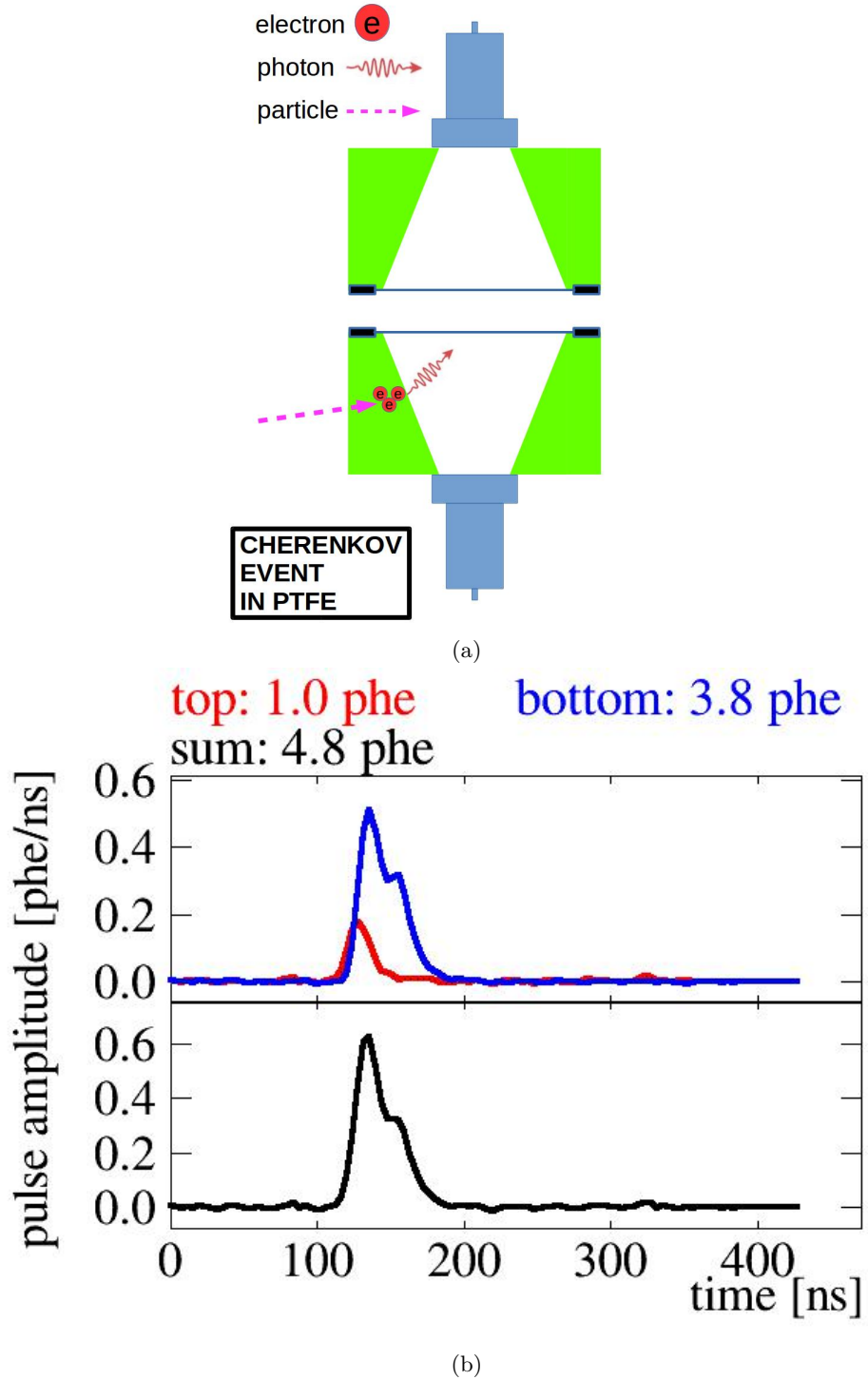


Figure 1.14: *Gas Test* extremely narrow event: (a) a cartoon for possible source: Cherenkov in PTFE (b) an example waveform. Data were taken at 2018-03-12 11:41 , with operation voltages V_T and V_B at 0 kV, operation detector gas density at vacuum.

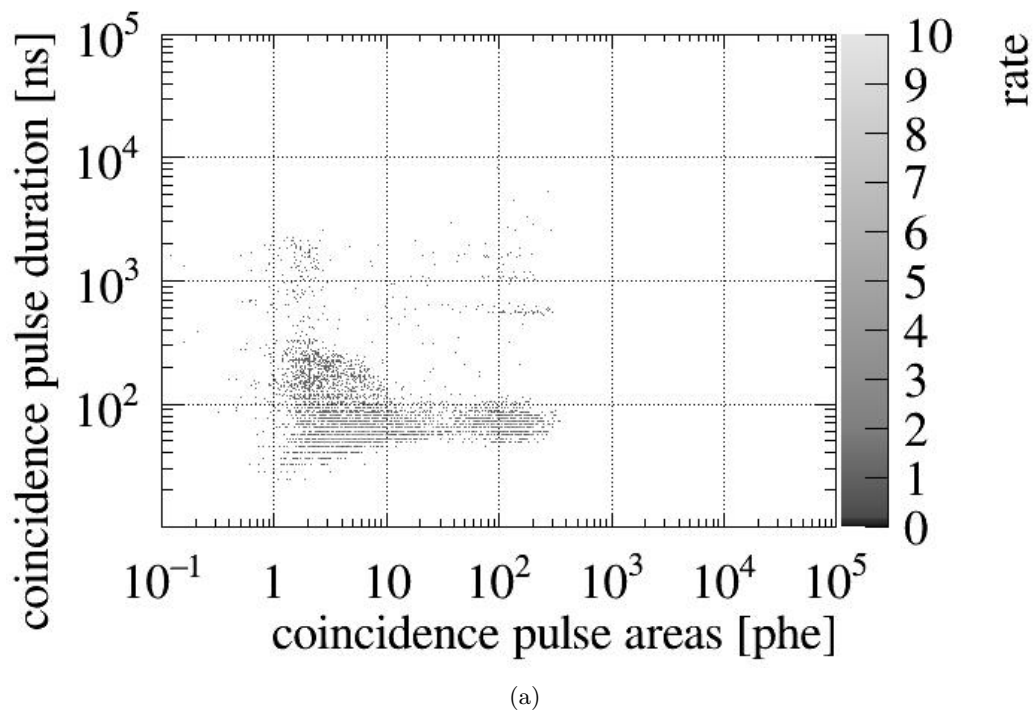


Figure 1.15: (a) vacuum data. Data were taken at 2018-03-12 11:41, with operation voltages V_T and V_B at 0 kV, operation detector gas density at vacuum. (b) xenon gas data. Data were taken at 2018-03-12 11:41, with operation voltages V_T and V_B at 0 kV, operation detector gas density at 0.137 mol L^{-1} .

⁹⁵⁵ **Appendix A**

⁹⁵⁶ ***Gas Test* RQ documentation**

⁹⁵⁷ This chapter summarizes the definitions of the RQs that are used for analysis in *Gas Test* analysis.

RQ name	shape	type	unit	default
‘aft_tXX’	array (L,)	float32	ns	nan
	Time difference between the start time of the pulse and the integrated pulse area reach XX% of the total area of pulse. XX=05,25,75,95.			
‘aft_t0’, ‘aft_t1’, ‘aft_t2’.	array (L,)	float32	ns	nan
	equivalent to ‘aft_t01’, ‘aft_t50’, ‘aft_t99’.			
‘arearq’	scalar	string		‘waveareas_trim_end’
	RQ used to compute coincidence pulse area.			
‘AmpThreshold’	scalar	float32	mV	2.5
	The threshold value for computing ‘above_threshold’ RQs.			
‘baselines’	array (L,)	float32	mV	nan
	Pulse baseline voltage.			
‘channels’	array (L,)	uint32		
	Pulse channel number.			
‘coin_pulse_amplitudes’	array (N,C)	float32	mV	nan
	Coincidence pulse amplitudes in each channel.			
‘coin_pulse_amplitudes_neg’	array (N,C)	float32	mV	nan
	Coincidence pulse negative amplitudes in each channel.			
‘coin_pulse_areas’	array (N,C)	float32	mV ns	nan
	Coincidence pulse areas in each channel.			

Continued on next page

RQ name	shape	type	unit	default
‘coin_pulse_areas_neg’	array (N,C)	float32	mV ns	nan
	Coincidence pulse negative areas in each channel.			
‘coin_pulse_areas_norm’	array (N,C)	float32	phe	nan
	Coincidence pulse area in each channel.			
‘coin_pulse_areas_post_TTus’	array (N,C)	float32	phe	0
	Pulse area of TT us after the stop time of a coincidence pulse. TT=100,50,20,10.			
‘coin_pulse_areas_pre_TTus’	array (N,C)	float32	phe	0
	Pulse area of TT us before the start time of a coincidence pulse. TT=100,50,20,10.			
‘coin_pulse_areas_section1’	array (N,C)	float32	phe	0
	Pulse area of a coincidence pulse of section1, which is defined by ‘pulse1_start’ and ‘pulse1_stop’.			
‘coin_pulse_areas_section2’	array (N,C)	float32	phe	0
	Pulse area of a coincidence pulse of section2, which is defined by ‘pulse2_start’ and ‘pulse2_stop’.			
‘coin_pulse_areas_sum’	array (N,)	float32	phe	nan
	Coincidence pulse total area.			
‘coin_pulse_areas_tXX’	array (N,)	float32	ns	nan
	Time difference between the start time of the coincidence pulse and the integrated coincidence pulse area reach XX% of the total area of the coincidence pulse. XX=01,05,10,15,25,50,75,85,90,95,99.			
‘coin_pulse_areas_tXXYY’	array (N,)	float32	ns	nan
	'coin_pulse_areas_tYY'-'coin_pulse_areas_tXX'			
‘coin_pulse_chs’	array (N,10)	int32		-1
	First 10 individual pulse channels in the coincidence pulse.			
‘coin_pulse_ids’	array (N,10)	int32		-1
	First 10 individual pulse ids in the coincidence pulse.			
‘coin_pulse_lastpulse_areas’	array (N,C)	float32	mV ns	nan
	Pulse area of the last pulse before a coincidence pulse in each channel.			
‘coin_pulse_lastpulse_ids’	array (N,C)	int32		-1

Continued on next page

RQ name	shape	type	unit	default
	Pulse id of the last pulse before a coincidence pulse in each channel.			
'coin_pulse_lastpulse_lens'	array (N,C)	float64	ns	nan
	Pulse length of the last pulse before a coincidence pulse in each channel.			
'coin_pulse_lastpulse_times'	array (N,C)	float64	ns	nan
	Start time of the last pulse before a coincidence pulse in each channel (since LZ_EPOCH_DATETIME).			
'coin_pulse_lens'	array (N,)	float64	ns	nan
	Coincidence pulse length.			
'coin_pulse_amplitudes_' peaktime	array (N,)	float64	ns	nan
	Time difference between the start time of the coincidence pulse and normalized coincidence pulse reach maximum amplitude.			
'coin_pulse_amplitudes_' peaktime_smooth	array (N,)	float64	ns	nan
	Time difference between the start time of the coincidence pulse and smoothed normalized coincidence pulse reach maximum amplitude.			
'coin_pulse_times'	array (N,)	float64	ns	nan
	Coincidence pulse start time (since LZ_EPOCH_DATETIME).			
'coin_pulse_waveforms'	list (N,C,W)	float32	mV	0
	Waveforms of a coincidence pulse in each channel.			
'coin_pulse_waveforms_norm'	list (N,C,W)	float32		0
	Waveforms of a coincidence pulse in each channel normalize by single photo electron size.			
'coin_pulse_waveforms_sum'	list (N,W)	float32		0
	Sum of waveforms of a coincidence pulse in all channels normalize by single photo electron size.			
'coin_pulse_wtime_tXXYY'	array (N,)	float32	ns	nan
	Pulse height(h_i) weighted average of time(t_i) between 'coin_pulse_areas_tXX' and 'coin_pulse_areas_tYY'. XXYY=1585, 0595. $\bar{t} = \sum h_i t_i / \sum h_i$.			
'coin_pulse_wtimeN_tXXYY'	array (N,)	float32	ns ^N	nan
	$\sum h_i (t_i - \bar{t})^N / \sum h_i$. XXYY=1585, 0595. N=2,3,4.			
'disp'	scalar	string		

Continued on next page

RQ name	shape	type	unit	default
	Display string ‘a:va;g:vg’. (ex: ‘a:+6.5;g:-6.5.’)			
‘duration’	array (F,)	float64	s	
	Duration of a file.			
‘dv’	scalar	float32	kV	
	Voltage difference between the top grid and the bottom grid.			
‘evtnum’	scalar	int64		
	Number of all computed pulses.			
‘firstvals’	array (L,)	float32	mV	
	Value of the first sample of the pulse.			
‘hft_t1’	array (L,)	float32	ns	
	Time difference between the start time of the pulse and the pulse amplitude reach maximum.			
‘in_coin_pulse’	array (L,)	bool		false
	Whether a pulse is in a coincidence pulse.			
‘neg_area_fraction’	array (L,)	float32		nan
	Ratio of negative pulse area and the sum of positive and negative pulse area.			
‘number_of_channels’	scalar	int32		4
	Number of channels.			
‘pos_area_above_threshold’	array (L,)	float32	mV ns	
	Pulse area above a certain threshold (default: 2.5 mV).			
‘pos_len_above_threshold’	array (L,)	float32	ns	
	Pulse length above a certain threshold (default: 2.5 mV).			
‘pos_len_above_threshold_- percentile_XX’	array (L,)	float32	ns	
	Time difference between the start of coincidence pulse of XX percent of all samples above a certain threshold. XX=05,50,95.			
‘pos_len_above_threshold_- trim_end’	array (L,)	float32	ns	
	Pulse length above a certain threshold excluding the ‘suppress_last_NSamples’ period.			
‘posareas’	array (L,)	float32	mV ns	
	Pulse positive area.			
‘pos_area_pulse1’	array (L,)	float32	mV ns	
	Pulse positive area of section1, which is defined by ‘pulse1_start’ and ‘pulse1_stop’.			
‘pos_area_pulse2’	array (L,)	float32	mV ns	

Continued on next page

RQ name	shape	type	unit	default
	Pulse positive area of section1, which is defined by ‘pulse2_start’ and ‘pulse2_stop’.			
‘pos_area_p1_p2’	array (L,)	float32	mV ns	
	‘pos_area_pulse2’ - ‘pos_area_pulse1’			
‘post_baseline’	array (L,)	float32	mV	
	Pulse baseline computed from the end of the pulse.			
‘post_pulse_length’	scalar	float64	ns	1800
	Pulse length not used in the end of a waveform for coincidence pulse searching.			
‘pre_baseline’	array (L,)	float32	mV	
	Pulse baseline computed from the beginning of the pulse.			
‘pre_pulse_length’	scalar	float64	ns	0
	Pulse length not used in the beginning of a waveform for coincidence pulse searching.			
‘procid’	scalar	string		
	Process id. (ex: [12345])			
‘prompt_frac_TTns’	array (L,)	float32		
	Ratio between the pulse area of the first TT ns and the total pulse area. TT=250,500,750,1000			
‘pulse1_start’	scalar	float64	sample	0
	Start time of pulse section 1.			
‘pulse1_stop’	scalar	float64	sample	75
	Stop time of pulse section 1.			
‘pulse2_start’	scalar	float64	sample	0
	Start time of pulse section 2.			
‘pulse2_stop’	scalar	float64	sample	200
	Stop time of pulse section 2.			
‘random_pulse_areas_post_TTus’	array (M,C)	float32	phe	0
	Pulse area of TT us after a random time. TT=100,50,20,10.			
‘random_pulse_areas_pre_TTus’	array (M,C)	float32	phe	0
	Pulse area of TT us before a random time. TT=100,50,20,10.			
‘random_pulse_times’	array (M,C)	float64	ns	nan
	A random time.			
‘rmsratio’	array (L,)	float32		

Continued on next page

RQ name	shape	type	unit	default
	Ratio between Root mean square (rms) of the waveform and the waveform amplitude.			
'sample_size'	scalar	float64	ns	4
	Sample size of a waveform.			
'skimfactor'	scalar	int64		1
	Ratio between the number of all computed pulses and the number of all recorded pulses.			
'sphe_size'	array (C,)	float64	mV ns	inf
	Pulse area of a single photo electron in each channel.			
'suppress_last_NSamples'	scalar	int32		450
	Number of samples not recorded in the end of a waveform.			
'times'	array (L,)	float64	ns	
	Pulse start time (since LZ_EPOCH_DATETIME).			
'trigvals'	array (L,)	float32	mV	nan
	Pulse trigger voltage.			
'usechannels'	array	int32		[0,2]
	Active channels.			
'va'	scalar	float32	kV	
	Voltage of the top grid.			
'vg'	scalar	float32	kV	
	Voltage of the bottom grid.			
'waveamplitudes'	array (L,)	float32	mV	
	Pulse amplitude.			
'waveareas'	array (L,)	float32	mV ns	
	Pulse area.			
'waveareas_trim_end'	array (L,)	float32	mV ns	nan
	Pulse area suppressing last 'suppress_last_NSamples' samples to 0.			
'waveforms'	list (L,)	float32	mV	nan
	Waveform.			
'wavelens'	array (L,W)	float32	ns	
	Pulse length.			
'window_width'	scalar	float64	ns	1500

Continued on next page

RQ name	shape	type	unit	default
	Window size of coincidence pulse searching. It is also called coincidence window width(CWW).			
'wtime'	array (L,)	float32	ns	nan
	Pulse height(h_i) weighted average of time(t_i). $\bar{t} = \sum h_i t_i / \sum h_i$.			
'wtimeN'	array (L,)	float32	ns ^N	nan
	$\sum h_i (t_i - \bar{t})^N / \sum h_i$. N=2,3,4.			
<p>L: number of all computed pulses. N: number of coincidence pulses. M: number of random pulses. C: number of channels. W: number of samples in a waveform. F: number of files in a dataset. LZ_EPOCH_DATETIME: 2015, Jan, 1st, 00 : 00 : 00. phe: average photo electron area.</p>				

Table A.1: Gas Test RQ documentation

₉₅₉ **Appendix B**

₉₆₀ **Abbreviations**

₉₆₁ This chapter summarizes the abbreviations that occur in this thesis.

₉₆₂ #: counts of

₉₆₃ ADC: Analog-to-Digital Converter

₉₆₄ BBN: Big Bang Nucleosynthesis

₉₆₅ CCD: Charge-couple device

₉₆₆ CMB: Cosmic Microwave Background

₉₆₇ CWW: Coincidence Window Width

₉₆₈ CV: Coefficient of Variation

₉₆₉ DAQ: Data AcQuisition

₉₇₀ DM: Dark Matter

₉₇₁ EL: ElectroLuminescence

₉₇₂ ELD: ElectroLuminescence Detector

₉₇₃ ER: Electron Recoil (event)

₉₇₄ LUX: Large Underground Xenon experiment

₉₇₅ LZ: LUX-ZEPLIN experiment

₉₇₆ MFC: Mass Flow Controller

₉₇₇ NR: Nuclear Recoil (event)

₉₇₈ PDE: Photon detection efficiency (also called light collection efficiency)

₉₇₉ PEEK: PolyEther Ether Ketone

₉₈₀ PHD(phd): counts of PHotoelectrons Detected

₉₈₁ PHE(phe): SPHE pulse area or counts of (single) PHotoElectrons. In other literatures, it is
₉₈₂ sometime called PE(pe).

₉₈₃ PMT: Photomultiplier Tube

₉₈₄ PTFE: PolytetraFluoroEthylene

₉₈₅ R&D: Research and development

- 986 RQ: Reduce Quantity of a pulse
987 S1: primary Scintillation light
988 S2: secondary Scintillation light
989 SS: Stainless Steel
990 Q.E.: Quantum Efficiency (of a PMT)
991 SLAC: SLAC national accelerator laboratory
992 TPC: Time Projection Chamber (detector)
993 WIMP: Weak Interaction Massive Particle
994 XML: eXtensible Markup Language
995 ΛCDM : Lambda Cold Dark Matter

⁹⁹⁶ Bibliography

- ⁹⁹⁷ [1] SAES, *PS3-MT3-R/N SPECIFICATIONS*, (2002) http://www.saespuregas.com/Library/documents/ps3spec_512.pdf.
- ⁹⁹⁸
- ⁹⁹⁹ [2] KNF Neuberger Incorporated Companies, *Diaphragm-Gas Sampling Pumps with double di-*
¹⁰⁰⁰ *aphragm System*, <https://www.knfusa.com/products/oem-products/product/products/diaphragm-gas-pumps-and-compressors/double-diaphragm-pumps/>.
- ¹⁰⁰¹
- ¹⁰⁰² [3] Alicat Scientific, *Operating Manual - MFCs*, http://www.alicat.com/documents/manuals/Gas_Flow_Controller_Manual.pdf.
- ¹⁰⁰³
- ¹⁰⁰⁴ [4] Hamamatsu Photonics, *Photomultiplier Tubes*, (2006) http://www.hamamatsu.com/resources/pdf/etd/PMT_handbook_v3aE.pdf.
- ¹⁰⁰⁵
- ¹⁰⁰⁶ [5] T. Shutt, *Light guide software for photon propagation (unpublished)*, (2018)
- ¹⁰⁰⁷ [6] J. W. Keto, R. E. Gleason, and G. K. Walters, “Production Mechanisms and Radiative Life-
¹⁰⁰⁸ times of Argon and Xenon Molecules Emitting in the Ultraviolet”, *Physical Review Letters*
¹⁰⁰⁹ **33**, 1365 (1974).
- ¹⁰¹⁰ [7] A. Hitachi et al., “Effect of ionization density on the time dependence of luminescence from
¹⁰¹¹ liquid argon and xenon”, *Physical Review B* **27**, 5279 (1983).
- ¹⁰¹² [8] F. P. Santos, T. H.V. T. Dias, A. D. Stauffer, and C. A. N. Conde, “Three-dimensional Monte
¹⁰¹³ Carlo calculation of the VUV electroluminescence and other electron transport parameters in
¹⁰¹⁴ xenon”, *Journal of Physics D: Applied Physics* **27**, 42 (1994).
- ¹⁰¹⁵ [9] A. Fonseca et al., “Study of secondary scintillation in xenon vapour”, in *Ieee symposium*
¹⁰¹⁶ *conference record nuclear science 2004*. Vol. 1, C (2004), pp. 572–576.
- ¹⁰¹⁷ [10] C. M. B. Monteiro et al., “Secondary scintillation yield in pure xenon”, *Journal of Instrumen-*
¹⁰¹⁸ *tation* **2**, P05001 (2007).
- ¹⁰¹⁹ [11] V. Chepel and H. Araújo, “Liquid noble gas detectors for low energy particle physics”, *Journal*
¹⁰²⁰ *of Instrumentation* **8**, R04001 (2013).

- 1021 [12] W. N. English and G. C. Hanna, "GRID IONIZATION CHAMBER MEASUREMENTS OF
1022 ELECTRON DRIFT VELOCITIES IN GAS MIXTURES", *Canadian Journal of Physics* **31**,
1023 768 (1953).
- 1024 [13] J. C. Bowe, "Drift Velocity of Electrons in Nitrogen, Helium, Neon, Argon, Krypton, and
1025 Xenon", *Physical Review* **117**, 1411 (1960).
- 1026 [14] J. L. Pack, R. E. Voshall, and A. V. Phelps, "Drift Velocities of Slow Electrons in Krypton,
1027 Xenon, Deuterium, Carbon Monoxide, Carbon Dioxide, Water Vapor, Nitrous Oxide, and
1028 Ammonia", *Physical Review* **127**, 2084 (1962).
- 1029 [15] H. L. Brooks et al., "Electron drift velocities in xenon", *Journal of Physics D: Applied Physics*
1030 **15**, L51 (1982).
- 1031 [16] T. Berghöfer, J. Blümer, and J. Hörandel, "A measurement of drift velocities of electrons in
1032 xenon–methane mixtures", *Nuclear Instruments and Methods in Physics Research Section A: Accelerators, Spectrometers, Detectors and Associated Equipment* **525**, 544 (2004).
- 1033 [17] V. F. Gachkovskii, T. A. Kudryavtseva, and N. M. Chirkov, "Dependence of the fluorescence
1034 intensity of polytetrafluoroethylene on the conditions of synthesis and molecular weight", *Bulletin of the Academy of Sciences of the USSR Division of Chemical Science* **18**, 2297 (1969).
- 1035 [18] P. Sorensen and K. Kamdin, "Two distinct components of the delayed single electron noise in
1036 liquid xenon emission detectors", *Journal of Instrumentation* **13**, P02032 (2018).
- 1037 [19] J. D. Jackson, *Classical Electrodynamics (3rd ed.)* (New York: John Wiley & Sons, 1999).